In-Situ Examination of the Development of Shear Localizations that Occur in High Strain Rate Compressive Loading in Steel

by

Michael Joseph Patrick Conway

A thesis submitted in partial fulfillment of the requirements for the degree of

Master of Science

Department of Mechanical Engineering

University of Alberta

Abstract

The objective of this thesis is to investigate material failure phenomena, specifically related to localizations with applications to naval and rail steels. In order to accomplish this objective, steels commonly used in naval and rail applications were examined in quasi-static and dynamic compression using a universal testing machine and a split-Hopkinson pressure bar, respectively, with in-situ imaging. The work was performed on two commonly used rail weights of 115 lb/yd and 136 lb/yd rail steel and a commonly used naval steel, HSLA 65. In this thesis, state-of-the-art ultra-high-speed imaging was used with testing procedures to visualize the deformation at high strain rates to capture phenomena that occur over microseconds to provide process information not readily available in the literature for the compressive stress-state. The quasi-static and dynamic tests were performed in compression to gain material behaviour in more representative strain rates and stress states of the steels in blast and impact loading. The in-situ imaging of the deformation process provided velocities, orientation and propagation of shear bands not widely reported in the literature with an appropriate experimental setup. The localizations that occur in the context of rail applications, is the white etching layer, which is a hardened layer that forms on top of the rail from repeated plastic deformation, heat and follows the development of shear banding. Process information was gained in regards to the formation of the white etching layer on the surface of the rail by displaying grain texturing not known to occur at low strains. The

new information found in this thesis was further discussed in context to the current understanding of shear banding and the formation of the white etching layer. Altogether, this work provides fundamental information for the validation of material models in studying high rate applications and use in industrial applications. It provides information into the current understanding of the shear banding and the white etching layer phenomena, improves understanding of material behaviour for design, and gives insight for the performance of the current materials commonly used in the naval and rail industries.

Preface

This thesis is an original work by Michael J. P. Conway. Chapter 3 and Chapter 4 have been prepared for publication in the Hypervelocity Impact Symposium (prepared for American Society of Mechanical Engineers (ASME)) and International Heavy Haul Associate conference proceedings, respectively. Chapter 3 is to be published as: "Michael J. P. Conway, J D. Hogan. Shear Band Characteristics in High Strain Rate Naval Applications", and Michael J. P. Conway performed the preparation, testing and analysis of the experiments with pre-existing equipment. I, Michael J. P. Conway, also drafted the manuscript and received feedback and approval from the co-author J D. Hogan for the final manuscript. Chapter 4 is to be published as: "Michael J. P. Conway, J D. Hogan, Michael Hendry. Dynamic and Quasi-Static Failure of Rail Steels", and Michael J. P. Conway performed the preparation, testing and analysis of the experiments with pre-existing equipment. Michael J. P. Conway also drafted the manuscript and received feedback and approval from the co-authors J D. Hogan and M. Hendry for the final manuscript.

For the examination of the naval steels, the work was financially supported by the Canadian Natural Sciences and Engineering Research Council, the Canadian Foundation for Innovation, and Defence Research and Development Canada. In studying the rail steels, the work was sponsored by the Canadian Rail Research Laboratory (CaRRL). CaRRL receives funding from the Natural Sciences and Engineering Research Council of Canada (NSERC), Canadian Pacific Railway, Canadian National Railway, the Association of American Railways – Transportation Technology Centre Inc., Transport Canada and Alberta Innovates.

Acknowledgements

I would like to thank my family for their unwavering support, discussions and motivation in completing this thesis and their support over my education. Without them the completion of this thesis would not be possible. I would also like to thank my supervisor Dr. Hogan for thoughtful discussions, support and feedback in both experimentation, analysis, ideas and writing. Further, I appreciate all the thoughtful conversations I have had with those that I've met along the way.

Contents

List of Tables

List of Figures

Nomenclature

Acronyms

AREMA American Railway Engineering and Maintenance-of-Way Association

ASB Adiabatic Shear Bands

CaRRL Canadian Rail Research Laboratory

DB Deformed Band

DIC Digital Image Correlation

DRX Dynamic recrystallization

HSLA High Strength Low Alloy

HVIS Hypervelocity Impact Symposium

HY Used for denoting a High Yield-Strength, for example steels such as HY-80 and HY-100

IHHA International Heavy Haul Association

NSERC Natural Sciences and Engineering Research Council of Canada

SHPB Split-Hopkinson Pressure Bar

TB Transformed Band

WEL White Etching Layer

Symbols

A_B	Area of bars	m^2
A_s	Area of specimen	m^2
C_B	Elastic wave speed in the bars	$\mathrm{m\,s}^{-1}$
E_B	Elastic modulus of the bars	GPa

L_s	Length of specimen	m
$\dot{\varepsilon}_s$	Strain rate in the specimen	s^{-1}
σ_s	Stress of the specimen	MPa
ε_r	Reflected wave strain	mm/mm
ε_s	Strain of the specimen	mm/mm
ε_T	Transmitted wave strain	mm/mm

Chapter 1

Introduction

1.1 Motivation

Steel is used in many industries including aerospace, rail, ship building, and automotive. The requirements of each industry can include considerations of the strength, ductility, weight, ease of manufacturing, and cost effectiveness. Two industries that have some similarities for steel requirements are the rail and ship industry that look for cost effectiveness, strength, and the ability to operate in a range of environments and loading conditions. Specifically, both industries require steels to operate in environments ranging from $-40\,^{\circ}\mathrm{C}$ to $40\,^{\circ}\mathrm{C}$, and handle high hydrostatic pressures as a consequence of buoyancy and contact forces. Further, a range of loading rates are experienced from impacts of the wheels at joints in the rail industry or explosions in combat situations for naval ships. In these cases, the strain rates are not limited to quasi-static loading and will commonly exceed $10^3\,\mathrm{s}^{-1}$ in normal operating conditions [1]. The need for higher strength steels is becoming increasingly common to resist the increasing loads (i.e. larger ships, higher capacity train cars) and speeds seen in the rail industry. Equivalently, these steel materials are required in the ship industry to maintain integrity of ships after impacts, whether it be in defence applications or servicing transportation routes such as ice breaking in Canadian waterways.

Generally, understanding the behaviour and failure of steels provides insight to produce and develop higher performing materials [2–4]. Some examples of

projects which would benefit from better understood steels would, first, be the rail industry in minimizing the maintenance and rail breaks. As of 2017, there is 61,859 km of rail operated in Canada [5] and, in this same year, a total of 369 Million Gross Tonnes (MGT) was transported on Canadian rail lines and is increasing [6]. Secondly, building and maintaining highly advanced naval ships is an ever increasingly important topic in Canada with large investments being made in the development of modern surface combatant ships with an expected value of $56 to $60 billion (CAD) [7]. These ships are the next generation of warships developed to provide protection of Canadian waters, and given their long service life, are expected to be technologically advance in materials, electronics and weaponry.

In all of these applications, a better understanding of the dynamic failure behaviour of steels is needed in order to develop improved predictive models for material performance in the extreme environments. This goes beyond simple, and sometimes not indicative, quasi-static material behaviour. This is because often the materials are operated outside of their quasi-static and linear elastic zones (post yield) and do not function in a single environment, but a multitude of environments that can drastically affect their performance after yield. One commonly studied failure mechanism that occurs in steel materials is shear banding [8–13]. A shear band is a shear localization in a material that forms, that impacts a materials ability to carry load, and is a precursor to cracking and failure [14, 15]. This phenomena is seen under many loading conditions, such as machining, forming, and high strain rate loading. In addition, these shear bands are not limited to metals, but form in a variety of materials such as metals [8, 14, 16], polymers [17], and geologic [18] materials. An example of the shape and form for application of these steels in their respective industries that are being investigated in this thesis are seen in Figure 1.1. In Figure 1.1a and Figure 1.1b are commonly used rail steels in light rail and heavy haul applications, respectively. The steel seen in Figure 1.1c is naval steel, HSLA 65, in the form it is seen on ships, albeit larger in ship production. Developing a fundamental understanding of how shear bands develop, in any form, and

(a) As-received profile of the a commonly used 115 lb/yd Canadian rail steel

(b) As-received profile of the a commonly used 136 lb/yd Canadian rail steel

(c) Commonly used HSLA 65 naval steel as-received plate

Figure 1.1. Collection of steels investigated in this thesis in their as-received form

alter a materials behaviour will have far reaching benefits to many research communities and industry. This topic is addressed in this thesis.

1.2 Thesis Objective

The objective of this thesis is to investigate in-situ localization phenomena in steels in compressive loading, with applications to rail and naval steels. To accomplish this objective we first investigate the length and time over which they form such as the size, rate and the dynamic conditions (i.e. strain rates) in which they occur, along with the stress-strain behaviour in both quasi-static and dynamic loading. Secondly, the deformation is characterized in-situ during quasi-static and dynamic compressive experimentation coupled with high-speed imaging, noting the shear banding and localizations that occur. This information is then linked with first-hand accounts of rail and naval steel failures, processes of formation, and real world phenomena such as the white etching layer that relates to shear banding in rail and naval applications. The information obtained in this thesis will provide new perspectives on processes of current failure mechanisms that are being researched and also provide spatial and stress-strain information for the development of material models predicting steel behaviour in high strain rate environments.

The thesis objective will be achieved by completing the following tasks:

1. Determine and select steel that show distinct localizations that are used in rail and naval applications.

2. Produce high quality tests of the chosen materials in quasi-static compression with in-situ imaging that provides strain information using Digital Image Correlation (DIC) and traditional compliance correction methods.

3. Test the materials in dynamic compression with in-situ imaging on materials determined to show localizations. This requires multiple tests to determine the rate of formation of the phenomena.

4. Quantify the localizations that occur on the surface and provide this information in the context of the formation processes of phenomena seen in real-world conditions.

5. Provide and relate the quantified localizations in context to validate models that predict shear banding.

1.3 Thesis Organization

This thesis is composed of four chapters. Chapter 1 provides the motivation for this research, the objectives and the organizational structure. Chapter 2 is a collection and review of the current state-of-the literature in relation to localizations that are seen at high strain rates and the by-products thereof. First, the steels examined in this thesis are explained with perspective of their use in their respective industry. Next, that chapter provides various theories proposed for the development of these localization phenomena, identification of their occurrence and information regarding the implications of their development. Lastly, it provides a brief overview of high strain rate testing of metals, the objectives of the apparatus', and perspective of the current methodology used in this thesis. Chapter 3 investigates the quasi-static and dynamic strength of HSLA 65, a high strength low alloy steel used in naval applications, using a universal testing machine and a split-Hopkinson pressure bar, respectively. In this chapter, the propagation velocity of shear bands that occur in quasi-static and dynamic conditions are documented and discussed. These velocities are captured using a high-speed and ultra-high-speed imaging to capture shear bands propagation at a frame rate of one million frames per second. Chapter 4 explores the quasi-static and dynamic behaviour of two commonly used rail steels and weights used in Canada; namely 115 lb/yd and 136 lb/yd. These experiments are visualized in-situ using ultra-high-speed imaging to capture localization and texturing related to the development of shear bands and the white etching layer, which is characterized and discussed in the context of the current understanding of the phenomena. Chapter 5 provides a summary of

the work completed in this thesis, along with the contributions made. Lastly, a compilation of future work is provided that would compliment the work completed in this thesis.

Chapter 2

Background

2.1 Materials

2.1.1 High Strength Low Alloy (HSLA) Steel

The development of High Strength Low Alloy steel mainly started in the 1950's and the 1960's from both an increased scientific understanding and a need of higher strength materials [19]. The scientific understanding allowing these set of steels to be made was specifically the effects of various elements added to the material. The commonly added elements are chromium, nickel, silicon, vanadium, titanium and zirconium [20]. An example of the composition of a high strength low alloy steel can be seen in Table 3.1 in Chapter 3. These components allowed for altering the corrosion resistance, strength, toughness, formability, weldability and ductility of the material [21]. In addition to having improved desirable characteristics, the cost of these materials lie between plain carbon steels and alloy steels, and thus, the cost performance of these steels is ideal for improving products in industries where exotic high strength materials are infeasible. Applications of high strength low alloy steels include oil and gas pipelines, rail and rail cars, off-shore buildings, and machinery [21]

One industry that benefits from high strength low alloy steel is in the construction of naval ships because of its relatively low weight, good weldability, higher toughness and ease of manufacturing in relation to formability [22, 23]. The alloying components can add characteristics of corrosion resistance, higher strength, better weldability and better manufacturing characteristics such as

stability during heating [21]. High strength low alloy steels have also been used in construction of naval ships since the mid 1950's [22, 24, 25], and since that time they have become the standard for naval ships [22]. Improvements in high strength low alloy steels from High Yield-Strength (HY) series of steel to HSLA allowed for less preheat, less care while welding and additional weight savings. The use of high strength low alloy steels are integral to many industries.

2.1.2 Rail Steels

The basic composition of rail steel and its pearlitic microstructure has remained the same as rails used in the early 1900's [26], and the increase in lifespan and track safety (i.e. preventing rail breaks) can be attributed to the quality control of rail steel in production and preventative rail maintenance. Quality control consists of, first, the infrastructure put in place in North America to have a basis on the expectations of a manufactured rail that is covered in the "Manual for Railway Engineering" [27], which also covers many other topics, but not limited to the design of roadway and ballast, ties and track. This document provides a basis of tolerances, production procedures, and testing requirements for manufacturers and purchasers to follow, and is a standard for rail sections used in North America; the standards are provided by the American Railway Engineering and Maintenance-of-Way Association (AREMA). Second, an increase of preventative maintenance of rail lines such as monitoring the rail for defects, rail grinding that is used to remove developing defects such as the white etched layer, corrugations, flaking, shelling or microcracks, and reducing the amount of impact loading on the rail (e.g. flange bearing crossings, continuously welded rail) have aided in preventing rail failures. To aid in withstanding the increased forces from higher loads and train speeds, the manufacturing techniques, material composition, the rail profile (cross-sectional area), and heat treatments have been altered and studied [26–28]. For example, bainitic rails [26], rail profiles, and thermomechanical processing [28] have been studied with success, but has not achieved wide spread adoption in industry because of unproven performance in large scale tests [26].

Rail steels are required to be high strength and ductile [29] for the large loads they carry at speed and the various terrain and climates they traverse. Rail steel is commonly fully pearlitic to provide the strength and ductility required while maintaining a good balance in cost. The cross-sectional areas have generally increased over time to support greater loads and, in North America, 115 lb/yd, 136 lb/yd and 141 lb/yd are commonly used [27]. These are categorized as a standard (310 HB) or high strength (370 HB) for a standard rail chemistry and a standard (310 HB), intermediate (325 HB) or high strength (370 HB) rail for a low alloy rail, which has a reduced carbon content range and a requirement of chromium [27]. Additionally, the use of head hardening has also produced rail that exhibits less wear than the non-head hardened counterparts [30].

2.2 Localization: Shear Bands

Shear bands are localizations that form in the material in dynamic or quasi-static loading [11, 31–34]. This is often seen as a competition between softening mechanisms and hardening mechanisms, reducing the load carrying ability [31]. Shear bands have been studied through experiments [9, 11, 15, 32, 35], and through computational and analytical modelling [36–40]. These experiments have looked at the microstructure after formation, propagation velocity [32, 35], temperatures [35], orientation to the geometry or microstructure [41], and the interactions with voids and subsequent cracking [14]. Outside of their developmental understanding, shear bands have been studied in many naval [10, 39, 42] and rail steels [8, 43]. One naval steel that exhibits localizations, specifically shear bands is HSLA 65 [39]. The localization form zones where deformation is concentrated and can be seen in Figure 2.1. The shaded lines on the surface of the specimen are locations where the shear band localizations occur and are seen to propagate at a 45° angle from the corners and perpendicular to the loading direction. These bands are analyzed for their propagation velocity and nucleation strain in Chapter 3.

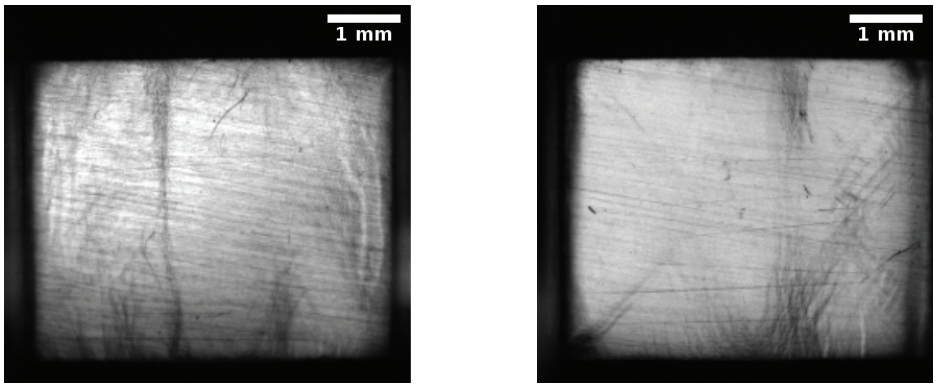

(a) (b)

Figure 2.1. Localizations seen on the surface of the HSLA 65 steel specimen during high strain rate compressive testing ($1800\,s^{-1}$) using a split-Hopkinson pressure bar

2.2.1 Formation Processes

The shear bands can commonly be classified as deformed shear bands and transformed shear bands [8, 9, 12, 13, 44], and these are mainly distinguished by whether the bands are resistant to etching and due to this resistance, they appears white using optical microscopy [11]. The formation of these bands are often geometry-dependent and defect dependent, meaning the shear bands often nucleate at a defect and develop along the direction of maximum shear stress [45, 46]. The first type of band is the deformed band. This band is denoted by the grains within the bands being mechanically sheared and elongated [47]. The adiabatic shears bands (ASB), which are the transformed bands, are seen as white etched bands in optical microscopy and are of high hardness. In Figure 2.2, an example of the band formation can be seen, which clearly exhibits the change in microstructure for each type of shear band. In Figure 2.2a, a deformed band is seen, denoted by the microstructure being mechanically deformed from going horizontal in the image to a diagonal within the band. It should be noted that the microstructure remains the same consistency as the rest of the sample. In Figure 2.2b, a transformed band is seen through the change in microstructure within the band in comparison with the bulk of the sample. Lastly, Figure 2.2c, shows the propagation of a shear band changing from a deformed band to a transformed band, which exhibits

its development process. These are formed at high strain rates, where the heat generated in the band is unable to be dissipated given the time scale that they occur. At this point, the heat generated and mechanical energy is dissipated in the recrystallization of grains [48]. Characterization of these shear bands carry many theories on the process of their development. These bands occur on a variety of widths ranging from 4 µm to 400 µm in metals [9, 15, 49].

The shear bands, while occurring at elevated strain rates, can also be seen to occur in quasi-static loading conditions in mild steel at the rates of $10^{-5}\,s^{-1}$ to $10^{-3}\,s^{-1}$, and occur as thin as 0.3 µm [33]. Shear bands have also been shown to be related to geometry, crystal structure, and microstructure for their propagation directions and initiation points [41]. Some theories of the shear bands formation processes include: dynamic recrystallization (DRX) [48], grain deformation [11], rotational recrystallization [50], and phase transformation [13]. These theories seek to explain formation processes of shear bands, which is a complex process with many different conditions dictating their generation for both categories of shear bands (deformed and transformed). The DRX theory [48] aims to explain the grain transformations that occur in adiabatic shear bands where the temperature rise from the plastic deformation is sufficient to create new recrystallized grains within the band. These new grains form in the size range of 10 nm to 100 nm and are recognized to be recrystallized due to the stress free and low dislocation density state [31]. Studies completed by

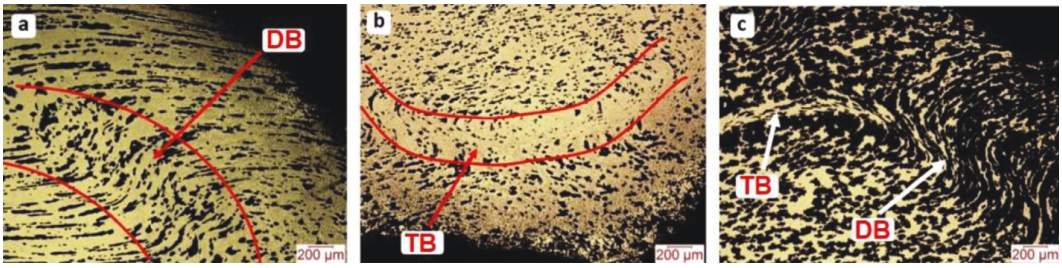

Figure 2.2. Microstructure progression of a deformed shear band into a transformed shear band (TB – Transformed Band; DB – Deformed Band). The above images show the elongation and deformation of the microstructure for deformed bands and supports the development of the deformed bands become transformed bands. This is shown by the propagation path and continuous nature of the development from mechanical deformation to transformation; Republished with permission [47]

Yang *et al.* [51] shows that there is evidence that this dynamic recrystallization does take place; the newly created grains that form in a transformed band can be seen to be elongated in the shear direction. This suggests that the recrystallization takes place while the band is still deforming and does not occur after the development of the shear band. Furthermore, evidence of grain boundary rotation is seen in the study by Yang *et al.* [51]. Grain boundary rotation allows for relaxation by allowing for lessening the grain boundary misorientation and thus creating a lower energy, more stable state. Yang *et al.* [51] suggests that both new grains are formed via DRX and the equiaxed grains are from static recrystallization from grain rotation, evidenced by two separate observable grains types after deformation. Another process that takes place in an adiabatic shear band is phase transformation [13]. This occurs from the temperature rise in the shear bands and usually occurs on the higher end of the spectrum of both strain rate and deformation incurred such as ballistic impact [47, 52]. In ballistic impacts, it has been seen that the temperature rise within the localizations can reach upwards of 1500 °C [53]. This temperature is high enough to support phase transformations and melting in AISI 4340 [52] and a carbon-manganese steel [54]. Further evidence of phase transformation is provided through numerical simulations [55] and carbide dissolution, producing a γ-iron and carbide mixture surround by nano-ferrite grains in pearlitic ultrahigh carbon steel [13].

2.3 Localization By-Product: White Etching Layer

A phenomena that is studied in the rail community is the white etching layer (WEL) that forms on the surface of the worn rail that is often an indicator of rail life and a precursor to rail breakage [56–59]. This layer forms on the top of the running surface of the rail and under optical microscopy appear white after applying an etchant (typically 3 % Nital). This layer can visually be seen on the surface of the rail, on the contact surface where the wheel and rail meet,

and is seen in Figure 2.3. In this figure, it should be noted that the WEL spots are elongated in the travelling direction and expand in thickness across the transverse direction, this has also been documented in other studies [60] along with the development of shear bands before WEL generation [46]. In practice, this layer is ground from the face of rail in regular operation to extend the life of the rail. The life of the rail is extended by performing this procedure due to the this layer being a nucleation site for of cracks and other defects which leads to the eventual failure of the rail [59].

The current understanding of the formation of the white etched layer is from high temperatures and/or large plastic deformation on the rail head as a consequence of repeated loading; the specific conditions in which they form are often studied are through numerical simulations [62]. The WEL is primarily composed of martensite [63], which requires the steel rail to develop temperatures above the austenization temperature ($> 700\,^{\circ}\mathrm{C}$) in operation and is rapidly quenched through conduction of heat in the bulk of the rail. Due to the time scales, and difficulties of observing these temperature rises and the deformation of the rail in-situ during experimentation, numerical simulations are useful tools in aiding to better understand how these phenomena develop. For example, in the white etching layer, the temperature rises are predicted to be lower in numerical simulations than what is required for the martensitic layer to form [62]. In numerical analysis by Ertz and Knothe [62], the temperature rise found of $200\,^{\circ}\mathrm{C}$ is not sufficient to produce martensite on the rail, which suggests that either the models do not capture the conditions accurately, or there are other processes that play a role in the development of the WEL. In the work by Ertz and Knothe [62], considerations of heat equilibrium between the wheel and ambient air, heat generation from sliding, and tread braking are used. Even with these considerations, it was found in the study by Ertz and Knothe [62], that WEL formation likely is not possible from heating alone. Further investigation into the heating from friction [56] exhibits a possibility that using values slightly outside the expected range of friction or slip produce conditions for the development of WEL. A Finite Element Method (FEM)

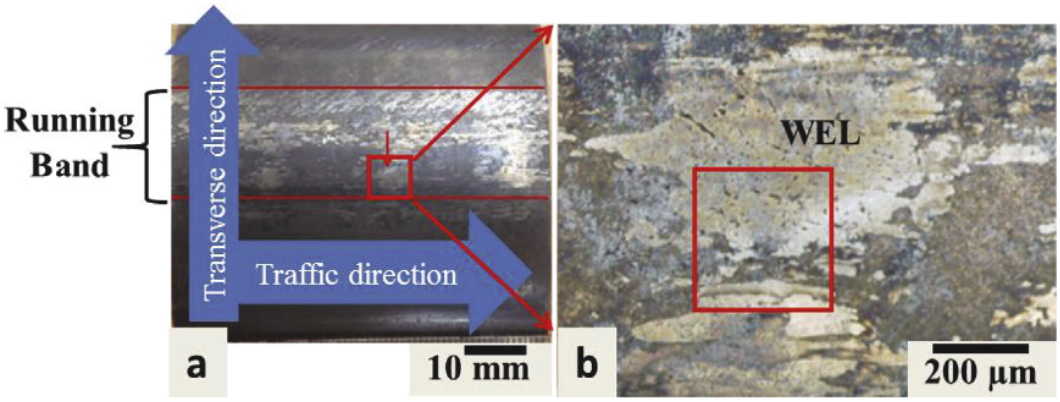

Figure 2.3. Visual inspection of the rail showing the formation of the WEL on the surface. The layer forms on the running surface between the wheel and rail parallel to the rolling direction. Republished with permission [61]

study conducted by Wu *et al.* [56] examined the thermomechanical behaviour and the contact between the rail and wheel. They examined the temperature rise on the rail surface with increased slippage. Slippage on the rail is when the velocity of the wheel at the contact point is not equivalent to the trains velocity, meaning the wheel is sliding on the rail to some degree. In this study, slippage between the wheel and the rail was increased to 3.6% of the 140 km h^{-1} velocity commonly used in Dutch rail lines and used a high coefficient of friction (0.6) to model higher roughness and conditions of the wheel just before fully sliding on the rail surface. Using their model, Wu *et al.* [56] that a peak temperature of 730 °C was obtained, and this temperature was above the austenization temperature of 700 °C at atmospheric pressure and 670 °C at a hydro-static pressure of 1.8 GPa (the pressure exerted by the rail wheel).

Alternatively, large plastic deformation is another suggested formation mechanism, in which nanocrystalline ferrite is formed [29] in the development of WEL. In the study by Lojkowski *et al.* [29], it is shown that from the examination of a worn rail that carbide dissolution occurred. To form the nanocrystalline structure that is found, the temperature for mechanical alloying need not to exceed 300 °C [29]. This then suggests that the high temperatures to reach austenization is not required to form WEL and instead large plastic deformation could potentially be the cause of the WEL forming on the surface. In both currently predicted formation mechanisms, the WEL can be identified

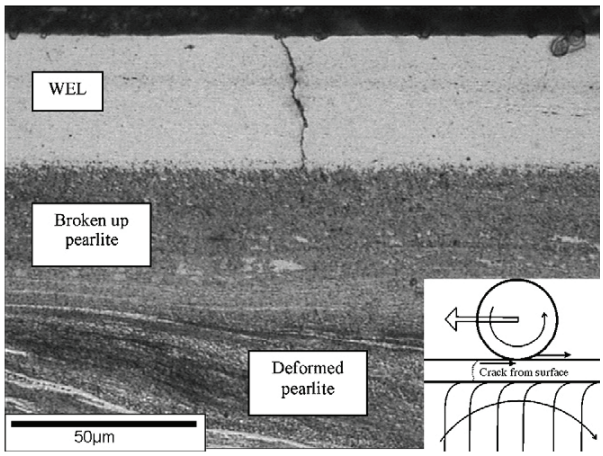

Figure 2.4. An optical microscopy image of a section of rail with WEL developed on the surface. This layer is seen to have cracks and the deformation on the surface is seen to affect the microstructure well below the WEL; Republished with permission [64]

as a hardened layer on the rail with a martensitic structure and spheroidized pearlite. This martensitic layer can achieve hardness exceeding 1200 HV [63, 65], and is often attributed to also having small grain size of less than a micron [61, 66]. The thickness of these WEL range from 10 µm to 30 µm [60, 66] with deformation reaching as deep as 3 mm [29] into the rail head. Consequently, the width of these bands are related to the contact patch of the rail and wheel [56, 60]. An optical microscopy image of the depth, cracking and deformation can be seen in Figure 2.4. In this image we see the extent of deformation from the rail-wheel contact, with plastic deformation of the pearlite seen well below the formation of the WEL. Secondly, the hardness of the WEL can be seen by the chipping on the rail surface, as well as the fracture extending to the broken up pearlite. This figure is overall a good example of many stages of progression of the WEL.

In addition to numerical studies, the generation of WEL has also been studied in a laboratory environment. Some mechanisms used to study the WEL generation are dry sliding wear test [67], rapid heating combined with cooling [56], and machining [68]. Generally, it is found that laboratory generation of the WEL is possible under these conditions, but is not exactly similar to what is found on used rail. One method for generating WEL in the laboratory is through dry sliding conditions, which is studied using twin-discs that are

pressed against each other with a press or jack and spun, similar to a gear mechanism. The pressure of contact and the amount of slip (i.e. velocities differing at the contact point) between the two discs then can be adjusted to reproduce similar conditions of the wheel and rail contact. In the study by Vargolici *et al.* [67], which employed the use of the twin-discs in dry sliding conditions, samples were prepared in various states, such as being oxidized. These were then tested with a 1 GPa contact pressure and a 0.5% sliding ratio between the discs. The simulated WEL produced in that study was not as hard as observed in real conditions and less wear was seen, compensated by increased plastic deformation. While the WEL produced was not exactly similar to what was produced in the real conditions, a layer of oxide was seen to effect the wear rate and development of WEL. Another method commonly used to study WEL formation experimentally is the rapid heating and cooling approach that is employed by Wu *et al.* [56], where heating rates of $20\,^{\circ}\mathrm{C\,s^{-1}}$ and $200\,^{\circ}\mathrm{C\,s^{-1}}$ were used and finally quenched at $67\,^{\circ}\mathrm{C\,s^{-1}}$. This setup attempts to simulate the fluctuation of temperatures on the rail when the wheel passes over and can be used with additional hydrostatic pressure in the heating and cooling cycles [56]. The hardness of this generated WEL was found to be lower than used rail, for example, the simulated WEL ranges from 670 HV to 810 HV in comparison with 725 HV to 1200 HV found on used rail [56]. Secondly, with smaller average grain sizes of the generated WEL at 269 nm, compared to the used rail at 272 nm, and while this difference is not large, the variation is seen in individual metrics. For example, the variation between the generated WEL and the WEL found on the used rail is better displayed by the largest grain diameter being 3.62 µm, in comparison with the largest grain diameter in the generated WEL being only 1.66 µm [56]. Another difference found was a larger portion of austenite existing in the microstructure in comparison with real world conditions [56]. These observations suggest that, while individual conditions can develop WEL separately, multiple conditions must exist simultaneously to produce WEL seen in previously used rail.

2.4 Linking White Etching Layer and Shear Bands

From the previous section (Section 2.3), the formation of the WEL is explained and, while the exact formation process is not exactly known, one area of research into the formation WEL consists of localizations such as shear banding [8, 46, 69]. One specific area of research is impact wear, which forms from the processes of impacting bodies and occurs at defects from the rail or wheel, joints and discontinuities on the rail. In a study performed by Zhang *et al.* [69], where a low alloy steel was repeatedly impacted, both shear bands and the WEL were found to form together. The experimental setup that was used was a 100 mm diameter hardened ball that was raised to a height of 3.5 m and allowed to freely fall and impact the surface of the steel. The impact surface was inclined to 45° and impacted up to 80 times in the same location on the steels surface. This was completed in two conditions, one with abrasive particles and the other on a clean surface. It was found that with as little as ten impacts, the WEL began to form and subsequent impacts, adiabatic shear bands were propagating from the WEL. Further, impacts were shown to initiate and propagate cracks along the adiabatic shear bands. Outside of experimentation, observations have been made that the propagation direction of shear bands also run parallel to the train motion, which suggests that these bands are further tempered into WEL (WEL is also parallel to train motion) [8]. The development of adiabatic shear bands and the white etching layer occur together with similar microstructures and characteristics as noted by Zhang *et al.* [46]. These two phenomena are widely studied in the literature and there has been evidence of shear bands leading to WEL formation. The literature does lack process-related information due to the difficulty of measurement related to the time scales and length scales that they form. It is then a benefit to investigate the individual processes that occur at appropriate length scales and the effect of impact (high rate loading) on the generation of WEL. This will be accomplished in this thesis.

2.5 High Strain Rate Testing

Mechanical testing can be categorized into multiple regimes that are reproducible by various testing techniques. For example, quasi-static strain rates range from $10^{-3}\,\mathrm{s}^{-1}$ to $1\,\mathrm{s}^{-1}$, intermediate strain rates range from $10^{1}\,\mathrm{s}^{-1}$ to $5\times10^{2}\,\mathrm{s}^{-1}$ and higher strain rates commonly obtainable in a lab environment are $10^{3}\,\mathrm{s}^{-1}$ to $10^{4}\,\mathrm{s}^{-1}$. Increasing the strain rate further to $10^{5}\,\mathrm{s}^{-1}$ to $10^{7}\,\mathrm{s}^{-1}$ can also be tested and involves shock wave propagation experiments (e.g. plate impact [70–72]).

Often, the split-Hopkinson pressure bar (SHPB) is used to test in the strain rates of $5\times10^{2}\,\mathrm{s}^{-1}$ to $10^{4}\,\mathrm{s}^{-1}$. This apparatus consists of a striker, incident and transmission bar. This apparatus is used to obtain the dynamic compressive response of materials. The dynamic response of a material is, for instance, when impacts of objects occur at high velocities. For example, the impacts in forging procedures, vehicle collisions, or projectiles hitting a surface at high velocity. High strain rates can invoke different responses in the material that is not limited to their ductile-brittle transition [73, 74], strength [39, 42], and elongation[75].

The split-Hopkinson pressure bar experimental setup, similar to what was used in this thesis, can be seen in Figure 2.5 and a typical direct impact Hopkinson pressure bar setup can be seen in Figure 2.6. The SHPB is often used to study shear bands that form at high strain rates [44, 50, 76] and is

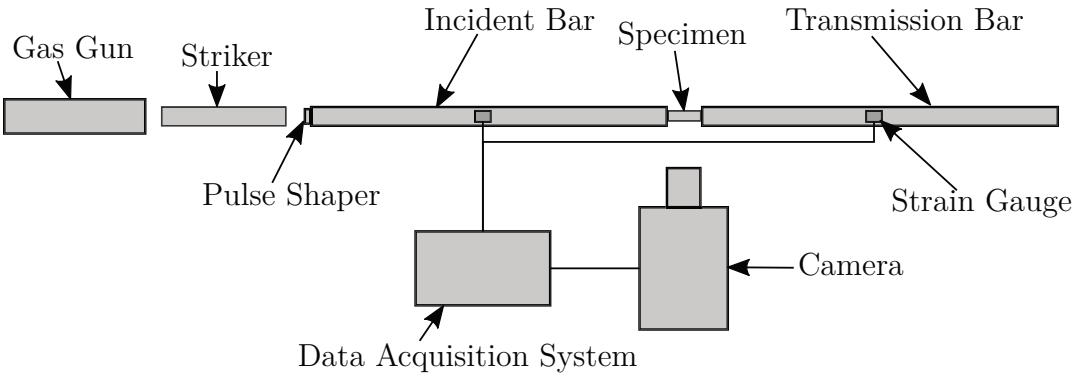

Figure 2.5. Illustration of a split-Hopkinson pressure bar apparatus system instrumented for recording in-situ deformation similar to the setup used in this thesis.

often completed through hat-shaped specimens [44, 77] or the use of a variation of the SHPB that removes the incident bar and directly impacts the specimen with the striker and records the signal in the output/transmission bar. The use of these techniques are two-fold, first to ensure shear band generation and second to reach high strain rates where adiabatic shear bands are likely to form. In general, a split-Hopkinson pressure bar as employed in Figure 2.5, consists of the components of a SHPB, in addition to a camera, data acquisition system and a pulse shaper. For the camera to capture the in-situ deformation of the sample, the camera is triggered after a set delay after the incident pulse travels through the strain gauge and is recorded in the data acquisition system. Next, the pulse shaper can be applied to reduce the amount of Pochhammer-Chree dispersion [78], improve stress equilibrium [79, 80] and provide a more constant strain rate over the test duration [79–81]. The stress equilibrium, which is an assumption made in the analysis of the data [81], can be verified through examining either the strain, stress or force at the interfaces of the bar and specimen and ensuring the differences between interfaces remains minimal over the course of the experiment. An example of this methodology can be seen in Section A.6, where the difference between the incident pulse and the added reflected and transmitted pulse is seen to be small over the duration of the test; this indicates a good test. Another assumption that is made in the analysis is a constant strain rate obtained during the test. This condition is met by the strain rate plateauing and remaining constant for the experiment after the initial loading, an example of this is seen in Figure A.14 of this thesis, and again, indicates a good experiment. Lastly, the incident pulse should be matched to the material response to minimize dispersion [82] and in aiding the previously mentioned two conditions [78, 79, 81, 83]. Further, the use of the equations governing the determination of the stress and strain of the material along with best practices used in this thesis can be found in Chapters 3 to 4.

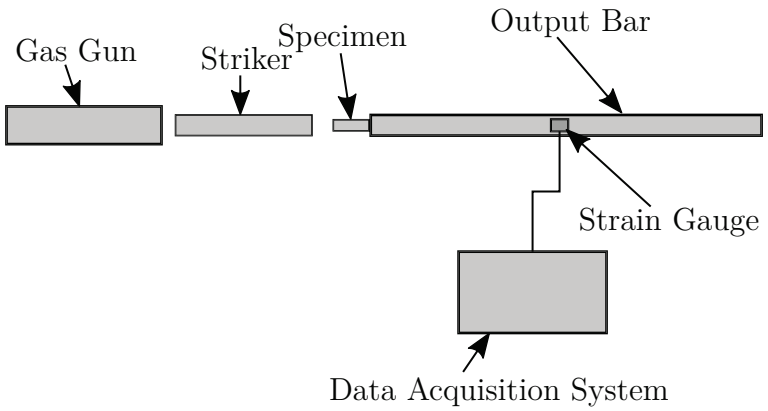

Figure 2.6. A direct impact Hopkinson pressure bar experimental setup for achieving higher strain rates, often used for the study of adiabatic shear bands

Chapter 3

Shear Band Characteristics in High Strain Rate Naval Applications

Accepted for publication in the Hypervelocity Impact Symposium conference proceedings published in the American Society of Mechanical Engineers (ASME) Journal with invitation for publication into the special issue of the International Journal of Impact Engineering (IJIE).

Abstract

This paper explores the dynamic behavior of HSLA 65 naval steels, specifically focusing on the initiation and growth of shear bands in quasi-static and dynamic compression experiments and how these bands affect stress-strain responses. The results indicate that the yield strength for HSLA 65 increases from $(541 \pm 8)\,\mathrm{MPa}$ for quasi-static $(10^{-3}\,\mathrm{s}^{-1})$ to $(1081 \pm 48)\,\mathrm{MPa}$ for dynamic rates $((1853 \pm 31)\,\mathrm{s}^{-1})$, and the hardening exponent increases from 0.376 ± 0.028 for quasi-static to 0.396 ± 0.006 for dynamic rates. Yield behavior was found to be associated with the onset of shear banding for both strain-rates, confirmed through visualization of the specimen surface using high-speed and ultra-high-speed cameras. For the quasi-static case, shear banding and yielding was observed to occur at 2.5% strain, and were observed to grow at speeds of upwards of $38\,\mathrm{mm\,s}^{-1}$. For the dynamic experiments, the shear banding begins at approximately $(1.18 \pm 0.06)\,\%$ strain and these can grow upwards of $(2122 \pm 213)\,\mathrm{m\,s}^{-1}$ during post-yield softening. Altogether, these measurements are some of the first of their kind in the open literature, and provide guidance on the critical time and length scales in shear banding. This information can be used in the future to design more failure-resistant steels, which has broader applications in construction, defense, and natural resource industries.

3.1 Introduction

Shear bands are an important topic in understanding the mechanics of materials as it is a dominant failure mechanism and precursor for crack initiation and propagation at high strain rates in many materials [14]. For example, shear bands are commonly observed in manufacturing and operation in the ship building [84], rail transportation [43], and aerospace industries [85]. In these industries, the materials are exposed to a wide range of strain rates from quasi-static to explosive loading. With the ever-increasing expectations of steels being stronger and more cost effective, it becomes more important to develop a fundamental understanding of the failure of these materials. In these applications, the formation of shear bands plays a role in the failure and the stability of the material. Understanding these loading conditions and the behavior of shear bands (i.e. velocity, propagation direction and propensity) will improve the material selection process and the performance of newly developed materials for these industries.

In the past, shear banding has been commonly observed in metals [8, 14, 16], polymers [17], and geologic [18] materials. Authors have studied shear banding through experiments [32, 35], and through computational and analytical modelling [36, 37]. Shear bands are commonly labelled as: 1. deformed shear bands, and 2. transformed shear bands, and these are mainly distinguished by whether a white etched hardened band is formed [11]. There has been several theories on the generation of shear bands in materials, including dynamic recrystallization (DRX) [48], grain deformation [11], rotational recrystallization [50], and phase transformation [13]. Regardless, shear bands are commonly believed to significantly affect material strength, stability, and have been noted to often be a precursor to cracking through the generation of voids [15]. Despite broad implications of shear banding to industry applications, the topic remains a very active area of research [14, 37, 86].

Motivated by these and many other past works, this paper focuses on studying the growth and evolution of shear bands in a high strength, low alloy steel,

specifically HSLA 65. We study material behavior through mechanical testing in compressive stress-states and couple this testing to visualization of shear banding and failure using high-speed and ultra-high-speed cameras and Digital Image Correlation (DIC) techniques. Being able to pair visualization and quasi-static and dynamic loading events provides insight into the deformation of the material and, specifically, the propagation velocity, direction, and orientation of the shear bands on the surface of the specimen. The results are discussed in the context of our current understanding of shear banding in steels, especially discussing the strains at which they occur, the velocity they grow, and their effect on the stress-strain response.

3.2 Methodology

3.2.1 Material Tested

HSLA 65 (ASTM A945 [23]) was tested in compression, where specimens were removed from the as-received steel plate that was 12" × 12" × 0.75" in size. This steel has been used on navy ships in Canada due to its cost effectiveness, weldability, and its high strength. The specimens were milled from the center of the thickness of the plate and were made in accordance with American Society for Testing and Materials (ASTM) standards following ASTM 09 for both specimen creation and testing. The HSLA 65 steel was specifically chosen due to the propagation of shear bands being clearly visible during the impact process. The chemical analysis of the HSLA 65 in this study is given in Table 3.1 and was provided from the manufacturer in the mill test certificate.

Table 3.1. Components of HSLA 65 (wt.% are listed)

C	Mn	P	S	Si	Cu	Ni	Cr	Mo	V	Ti	Al	Cb	N
0.08	1.43	0.02	0.004	0.299	0.02	0.01	0.04	0.006	0.067	0.016	0.03	0.035	0.008

3.2.2 Quasi-static Testing

Compression tests were performed on a MTS 810 testing machine for rectangular specimens of size 5.00 mm × 4.00 mm × 3.50 mm using displacement control. The quasi-static tests were performed at a nominal strain rate of $10^{-3}\,s^{-1}$. This specimen shape was selected for the ability to visualize the deformation on the surface of the specimen during experiments, as well as to perform measurements using Digital Image Correlation. The displacement and force were recorded through the MTS machine at a sampling rate of 100 Hz, while the surface and deformation features of the specimen were recorded through the use of a PROMON one-megapixel camera with a macro lens recording at 100 frames per second, which matched the sampling frequency of the MTS machine. The strains were measured during testing using DIC techniques with the VIC2D commercial software. This approach consisted of applying a randomly distributed pattern over the surface of the specimen using an airbrush and trying to minimize the overall particle size through atomization given the small specimen size. This was achieved through the use of an ultra-fine point airbrush to apply black paint that resulted in a speckle diameter between 50 and 300 microns. The quality of the speckle pattern was checked in the VIC2D software to minimize error before experimentation. During testing, an ultra-bright LED light equipped with a 7.6 mm diameter liquid light guide was used to illuminate the specimen in a highly contrasted and overexposed condition. Once the data was obtained, the DIC data was paired with the captured load data from the universal testing machine and matched to the DIC strain data through physical events captured in both measurement techniques. In this case, a sharp unload was induced, which was matched in time between the camera and MTS measurements. Using DIC, both small strains and large plastic strains can be resolved, whereas conventional strain gauges cannot be used to provide similar measurements [87] without the need to apply compliance corrections for the universal testing machine. Additionally, a greater amount of data can be derived from the measurements given the ability to spatially resolve the strain across the surface of the specimen providing information such

as local strains, displacement and ultimately verifying stress equilibrium.

3.2.3 Split-Hopkinson Pressure Bar Testing

A Split-Hopkinson Pressure Bar (SHPB) was used to perform dynamic compression measurements. The same specimen sizes were used in the dynamic experiments as the quasi-static experiments (5.00 mm × 4.00 mm × 3.50 mm), and the rectangular shapes were chosen for visualization purposes. The apparatus consisted of a 304.8 mm striker, 914.4 mm incident bar and a 1016 mm transmission bar that all have a diameter of 12.7 mm. The bars are made of Maraging C350 steel that has a minimum hardness of 52 HRC. The SHPB is an apparatus that takes an input from a striker that is fired from a gas gun. The striker then impacts a pulse shaper that is attached to the incident bar. This pulse shaper is used to shape the profile of the input pulse to achieve proper stress equilibrium and constant strain rate in the specimen [81]. In our experiments, mild steel with a diameter of 6.35 mm and a thickness of 0.635 mm was used, which follows from previous studies on improving stress equilibrium and reducing Pochhammer-Chree dispersion during SHPB testing [78, 88]. The specimen and the pulse shaper are both placed with a small amount of high pressure grease to minimize friction between the interfaces [81]. Verification of stress equilibrium is performed through a force balance, which is found in reasonable agreement for all our tests. In these experiments, the surface of the specimen is recorded using a Kirana ultra-high-speed camera with a HBM GEN3i data acquisition system recording at 20 MHz. The data acquisition triggers the camera from the beginning rise of the incident pulse and the camera trigger pulse is recorded in the data set. The camera records 180 frames at 1 million frames per second with a resolution of 924 pixels x 768 pixels. At this frame rate and resolution, we can visualize deformation in materials at sufficient spatial and temporal resolution that are not widely reported in the literature.

3.3 Results

In this study we investigate the compressive behavior of HSLA 65 navy steel in quasi-static and dynamic loading conditions. To begin the analysis, we have shown three stress-strain curves for the quasi-static case and four stress-strain curves for dynamic case in Figure 3.1 to demonstrate the rate-effects and repeatability of the measurements. In quasi-static testing conditions at a strain rate of $0.001\,\mathrm{s}^{-1}$, the yield strength of the HSLA 65 was found to be $(541 \pm 8)\,\mathrm{MPa}$, which are colored black in Figure 3.1. The yield stress found at a dynamic strain rate of $(1853 \pm 31)\,\mathrm{s}^{-1}$ was $(1081 \pm 48)\,\mathrm{MPa}$ (colored blue in Figure 3.1). These values are summarized in Table 3.2. The yield strengths and symmetrical limits are found from averaging the resulting values in each test and providing the standard deviation across the sample set. In quasi-static and dynamic loading of HSLA 65, there is a distinct yield point seen in the curves. For the quasi-static experiments, the yield strain is $(0.93 \pm 0.12)\,\%$ and for the dynamic experiments, the yield strain is $(1.05 \pm 0.03)\,\%$. At the higher strain rates, this yield point is much more prominent, while the Pochhammer-Chree dispersion should be considered after the yielding of the material. Later, these yield features are linked to shear banding and failure in the material.

To further probe material behavior and generalize the results, the flow stress for this material was calculated using the true stress-true strain data for Equation (3.1).

$$\sigma_f = K\varepsilon^n \tag{3.1}$$

where the flow stress, σ_f, is the stress required to continue the plastic deformation of a metal. From Equation (3.1), K is the strength coefficient, ε is the plastic strain, and n is the hardening coefficient. Using a linear fit of the true strain-true stress data on a log-log scale [89], the strength coefficient for the quasi-static case is $K = (2029 \pm 172)\,\mathrm{MPa}$ with a strain hardening coefficient of $n = 0.376 \pm 0.028$. For the dynamic experiments, the strength coefficient is found to be $K = (3098 \pm 52)\,\mathrm{MPa}$ and the hardening coefficient

is $n = 0.396 \pm 0.006$. These values are also summarized in Table 3.2 for both strain rates, along with the yield strength.

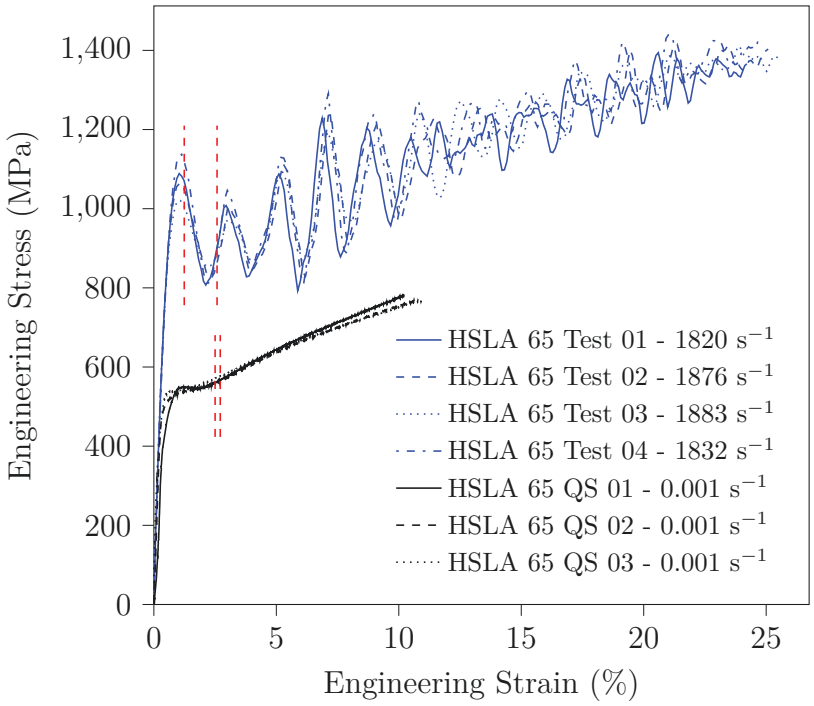

Figure 3.1. Engineering stress-strain curves of the tested HSLA 65 in quasi-static (black) and dynamic (blue) compression. The vertical lines indicate the region that shear band measurements were taken, which are linked with subsequent figures.

Table 3.2. Flow stress coefficients for HSLA 65 in quasi-static and dynamic compression.

Strain Rate (s^{-1})	Yield Strength (MPa)	K (MPa)	n
0.001	541 ± 8	2029 ± 172	0.376 ± 0.028
1853 ± 31	1081 ± 48	3098 ± 52	0.396 ± 0.006

Next, we investigate a series of high-speed camera images for the quasi-static experiments, which are shown in Figure 3.2, and dynamic experiments that are shown in Figure 3.3. In Figure 3.2, the collection of images were chosen that represents notable stages in shear band development in the quasi-static experiment: Figure 3.2a shows the intact surface before localizations occur; Figure 3.2b shows localizations forming on the surface at 45° to the loading direction with the predominant bands developing from the edges and propagating inwards until they meet; Figure 3.2c shows the surface at which

point the bands visually look consumed by the surface texturing that begins to develop at later stages of plastic deformation. The localizations began forming on the surface at approximately 2.5% strain. Next, shown in Figure 3.3 are a collection of high-speed camera images taken during a dynamic experiment that demonstrate the initiation and growth of shear banding. The top left image Figure 3.3a shows the specimen in pristine conditions. Figure 3.3b shows the surface at ∼1% strain with the initial bands propagating across the surface. The initiation of the localizations occurs at the corners of the specimen and again propagate at approximately 45° angles. Across all the dynamic experiments, the initiation of these localizations on the surface begin at approximately $(1.19 \pm 0.06)\,\%$ strain. In comparison with the stress-strain curve (Figure 3.1), the localizations approximately begin around the yield of the material. Further, Figure 3.3c shows the specimen surface at ∼2% strain, and this is when the bands begin to coalesce on the surface that is shown. The bands are the most visually distinct at this strain. At later strains (Figure 3.3d), we observe surface texturing occurring that consumes the shear bands on the surface and this continues until only the large and visually distinct localizations can be seen, which remain after the experiment. This occurs similarly to the quasi-static experiments (Figure 3.2c).

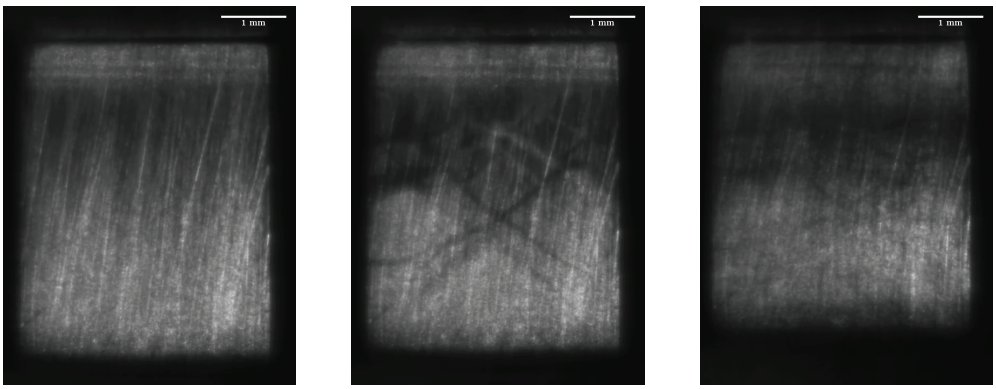

(a) (b) (c)

Figure 3.2. Surface of HSLA 65 specimen in quasi-static compression using a MTS 810 universal testing machine at a strain rate of $10^{-3}\,\mathrm{s}^{-1}$: Image a) surface of the specimen before deformation; b) surface of the specimen with localizations fully developed at ∼4.6% strain; and c) surface of the specimen after formation of bands as surface texturing develops at ∼11% strain demonstrating that the shear bands are consumed and are barely visible.

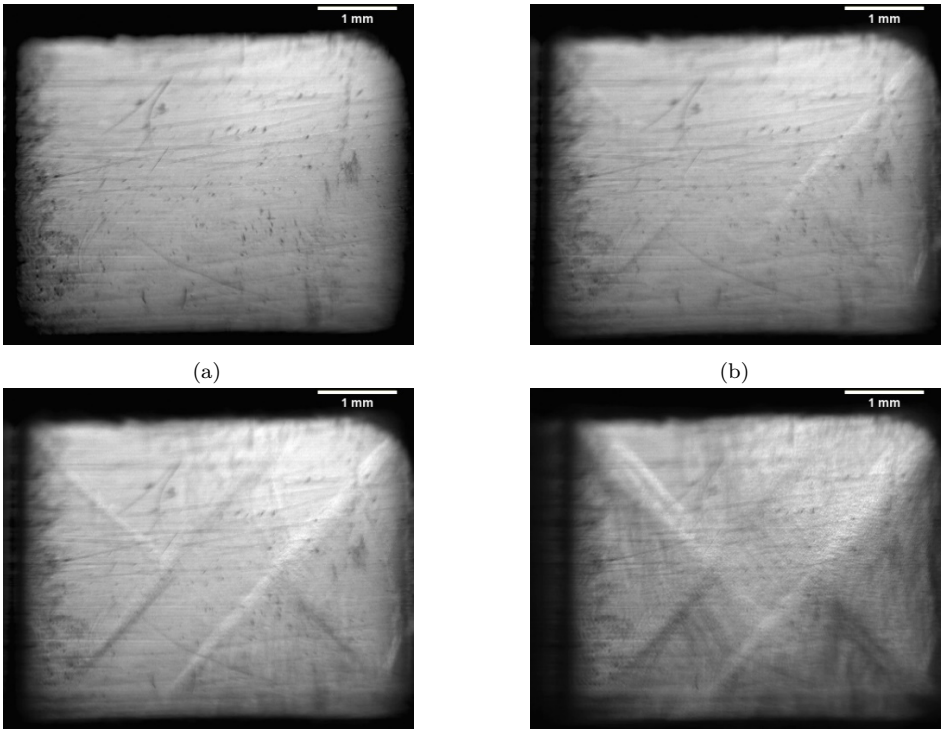

Figure 3.3. In-situ images of HSLA 65 using Kirana ultra-high-speed camera filming at 1 million frames per second in a Split Hopkinson pressure bar testing apparatus: a) surface of specimen prior to deformation; b) surface of specimen with bands beginning to form at ∼1% strain; c) surface of specimen with bands formed before coalesce dominates at ∼2% strain; d) surface of specimen with visible localizations and surface texturing at ∼3.9% strain.

Using ImageJ [90, 91], the initiation and growth of shear bands were tracked over multiple frames for both quasi-static and dynamic loading. The velocity of the localizations on the surface is plotted against the compressive strain for both strain rates in Figure 3.4, with the range of the strain they occur over denoted in Figure 3.1 as red vertical lines. The measurements were taken until the originally pristine surface was filled with the larger bands. At this point, coalescence is predominant and the resulting shear bands are not included in the analysis. In the quasi-static case, the shear bands begin to form on the surface at approximately 2.5% strain and accelerate from a velocity of $(27 \pm 5)\,\mathrm{mm\,s^{-1}}$ to $(38 \pm 8)\,\mathrm{mm\,s^{-1}}$ at a strain of 2.51%. Following this, the band growth slows to $(19 \pm 4)\,\mathrm{mm\,s^{-1}}$ and stays approximately constant over the next 0.01% strain, at which it slows to $(11 \pm 2)\,\mathrm{mm\,s^{-1}}$ before meeting other localizations seen on the surface at a strain of 2.71%. Again, these measurements are shown as black dots in Figure 3.4.

For the dynamic case (blue dots in Figure 3.4), the shear bands are tracked from ∼1.24% to ∼2.58% strain, and this occurs approximately over 4 µs during the experiment. The shear band velocity measurements for the dynamic cases are shown as black points in Figure 3.4. In this plot, the error bars correspond to the bias uncertainty in the calculation, including the camera resolution, variation in time for each frame, and in the dynamic case the random error in repeated measurements of the length of the band between experiments. These errors provide the variation in calculated shear band growth velocities given the short time scales over which they are calculated. The first measurement of velocity is $(951 \pm 96)\,\mathrm{m\,s^{-1}}$ at approximately 1.24% strain, where the growth of the band accelerates for the next two frames to $(1911 \pm 192)\,\mathrm{m\,s^{-1}}$ at 1.46% strain and $(2122 \pm 213)\,\mathrm{m\,s^{-1}}$ at 1.92% strain. At the third frame, the band growth begins to decelerate, when it reaches approximately 2% strain and finally ends at $(1464 \pm 147)\,\mathrm{m\,s^{-1}}$. After this time, the bands may arrest after fully forming on the surface and the energy may be transformed into heat, further deformation and grain alterations [92]. Relating the strain measurement from the images to the stress-strain curves, the pace of growth begins and increases

at the point of yield and slows near the trough of the softening (Figure 3.1). Generally, the velocity first accelerates as new bands begin forming on the surface and decelerates until coalescence begins.

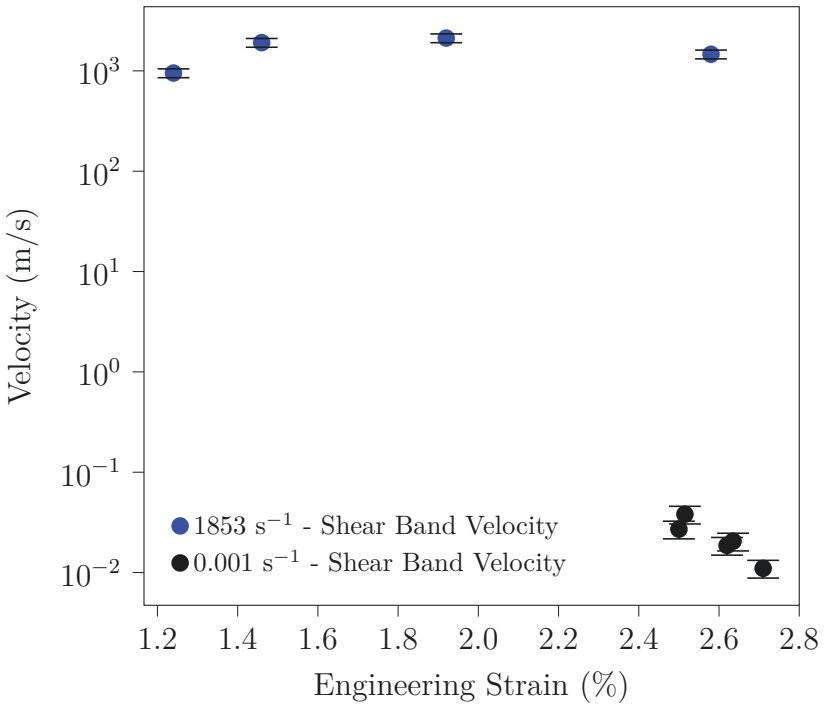

Figure 3.4. Velocity of shear bands on the surface of the specimens in quasi-static and dynamic compression where the first and last points for each respective case correspond to the lines on the stress-strain curve provided in Figure 1

3.4 Discussion

In this paper, we explored the strain rate-dependent compression response of HSLA 65 naval steel, focusing on shear bands and failure. Consideration of the stress-strain response found that the yield strength is (541 ± 8) MPa for quasi-static and (1081 ± 48) MPa for dynamic rates, the K is (2029 ± 172) MPa for quasi-static and (3098 ± 52) MPa for dynamic rates, and the hardening exponent n is 0.376 ± 0.028 for quasi-static and 0.396 ± 0.006 for dynamic rates. These measurements are consistent with those reported in the literature for HSLA 65 [39], and they demonstrate that the HSLA 65 steel is comparable to common naval steels such as HY-80 [93] and DH36 [42].

To explore material responses further, mechanical testing was coupled to high-speed imaging of the specimen surface to investigate shear banding and failure in HSLA 65. To do this, the initiation and growth of the bands were tracked using ImageJ, and the resulting growth rates were plotted against compressive strain (Figure 3.4). In the quasi-static case, the shear bands begin to form on the surface of the specimen at approximately 2.5% strain and accelerate to a peak of $(38 \pm 8)\,\mathrm{mm\,s^{-1}}$ at a strain of 2.51%. Following this, the band growth slows to $(19 \pm 4)\,\mathrm{mm\,s^{-1}}$ and stays approximately constant over the next 0.01% strain, at which it slows to $(11 \pm 2)\,\mathrm{mm\,s^{-1}}$ before coalescing with other localizations observed on the surface at a strain of 2.71%. For dynamic strain rates of $(1853 \pm 31)\,\mathrm{s^{-1}}$, the bands begin to grow at approximately 1.2% strain, and they accelerate up to $(2122 \pm 213)\,\mathrm{m\,s^{-1}}$ at 1.9% strain. Following this, the bands decelerate and then are consumed by deformation on the surface of the specimen. Relating the strain measurement from the images to the stress-strain curves, the pace of growth begins and increases at the point of yield and slows near the trough of the softening (see Figure 3.1 and Figure 3.4). Altogether, results from this paper will be important in the development of models, both for phenomenological [94] and for those models that capture shear banding in steels [95, 96].

The peak velocity of $(2122 \pm 213)\,\mathrm{m\,s^{-1}}$ is 68% of the shear wave speed, which is acceptable to values of 40% to 67% that are commonly reported in the literature [32, 35, 97]. While numerical simulations show generally good agreement with experimental studies, shear band velocities in simulations have been shown to be higher using methods which do not require mesh generation [97]. In the study by Li *et al.* [97], a better curvature match is found in regards to Zhou *et al.* [35] experimental work, although the peak velocity was found to be $2005\,\mathrm{m\,s^{-1}}$ with an impact velocity of $35\,\mathrm{m\,s^{-1}}$. Coupled with the current work, it may be plausible that the shear bands can meet or exceed previously found velocity values in the experimental literature. Namely, the shear band velocities found in this study are higher than those velocities found in studies relating to Maraging c300 steel by Zhou *et al.* [35], who found at a

peak velocity of $1200\,\mathrm{m\,s^{-1}}$ with the same acceleration pattern that was found in this study even given the smaller time window our measurements exist within. In a separate study by Guduru *et al.* [32] also using Maraging c300 steel found the peak velocity to be $1100\,\mathrm{m\,s^{-1}}$, although they found that the generated shear band momentarily slowed down and then proceeded to accelerate again. This behavior is not seen in our current work or in the work of Zhou *et al.* [35]. Our study also did not observe fracturing from the shear band, which was noted in the works by Zhou *et al.* [35] and Guduru *et al.* [32].

3.5 Concluding Remarks

In this paper, we investigate the dynamic failure and shear banding in HSLA 65 steel. To accomplish this, we performed strain-rate dependent compression measurements on the material and coupled high-speed and ultra-high-speed cameras to monitor the initiation and growth of shear bands during testing. These observations were linked to measurements of the stress-strain response of the materials. Results indicate that the yield strength increases from $(541 \pm 8)\,\mathrm{MPa}$ for quasi-static ($10^{-3}\,\mathrm{s^{-1}}$) to $(1081 \pm 48)\,\mathrm{MPa}$ for dynamic rates ($(1853 \pm 31)\,\mathrm{s^{-1}}$), and the hardening exponent increases from 0.376 ± 0.028 for quasi-static to 0.396 ± 0.006 for dynamic rates. The yield in the material was observed to be associated with the onset and evolution of shear banding in HSLA 65. For the quasi-static case, shear banding and yielding was observed to occur at 2.5% and $(0.93 \pm 0.12)\,\%$ strain, respectively and these can reach speeds of upwards of $38\,\mathrm{mm\,s^{-1}}$. For the dynamic experiments, the shear banding begins at approximately $(1.18 \pm 0.06)\,\%$ strain and these can grow upwards of $(2122 \pm 213)\,\mathrm{m\,s^{-1}}$. Altogether, this study provides new insights into shear banding and dynamic failure of steel materials, which is useful in manufacturing and modelling of these materials.

3.6 Acknowledgements

This work is supported by the Canadian Natural Sciences and Engineering Research Council, the Canadian Foundation for Innovation, and Defence Research and Development Canada. Calvin Lo and Haoyang Li are thanked for their aid while running the experiments.

Chapter 4

Dynamic and Quasi-Static Failure of Rail Steels

To be published in the International Heavy Haul Association (IHHA) conference proceedings.

Abstract

Mechanical behaviour at high strain rates and representative stress-states becomes important in many cases in rail transport, especially at zones that experience high impact loading. In this work, the behaviour of railway steel is probed for compressive stress states at quasi-static ($10^{-3}\,s^{-1}$) and dynamic ($10^{3}\,s^{-1}$) strain rate is examined with in-situ imaging using a MTS 810 universal testing machine and a Split-Hopkinson Pressure Bar, respectively. This was completed for two railway steels commonly used in Canada: 115 lb/yd and 136 lb/yd rail weights. The selected 115 lb/yd rail exhibited more thermal softening in dynamic loading and an increase in yield strength from $(934 \pm 71)\,MPa$ to $(1528 \pm 86)\,MPa$ when going from quasi-static ($10^{-3}\,s^{-1}$) to dynamic conditions ($1062\,s^{-1}$). Similarly, the 136 lb/yd yield strength increased from $(623 \pm 56)\,MPa$ at $10^{-3}\,s^{-1}$to $(925 \pm 67)\,MPa$ at $1199\,s^{-1}$. From the high-speed images, texturing is seen on the surface of both rail steels occurring corresponding to the yield of the material and subsequent thermal softening. This texturing is important in the study of the White Etched Layer (WEL) and shear banding.

4.1 Introduction

Understanding the mechanical response of rail steel has been shown by many in the literature to be important for understanding the in-use rail performance [98]. Commonly, the characterization of rail steel is completed through tensile testing, hardness testing and evaluating the wear patterns on used rails [27]. While these characteristics are important for identifying rail steels that will have acceptable performance, little work has been completed to examine the mechanical response at high strain rates and for compressive stress-states [8, 43, 99], despite these conditions being important in the contact and impact loading applications experienced in rail transport. More specifically, dynamic and impact loading is often seen at bolted rail joints, crossings, and switches. Evidence from the literature suggests that dynamic loading increases the accumulation of wear and frequency of maintenance through increased stresses seen on the rail surface [100]. This increased wear increases the occurrence of defects, and ultimately catastrophic failure. Impact loading is recognized as an issue that aids in increased deterioration of the rail and is actively being reduced through, for example, the use of flange bearing transitions at crossings [101]. While decreasing the occurrence of impact loading in as-designed track, this does not eliminate the need for understanding the behaviour of the rail in impact loading as it is still commonly found from defects such as flat wheels or damaged rail [1]. To address this gap in knowledge, this paper examines the strain-rate dependent behaviour of rail steel, focusing on understanding rate effects on failure and mechanical properties.

Few studies have focused on the dynamic failure of rail steel [8, 43, 99]. One related and commonly studied phenomena associated with the dynamic behaviour of rail steel is the white phase existing on the surface of previously worn rail head [56–58]. This phenomena is often a precursor to rail breakage as it serves as sites for crack nucleation [59]. The current understanding of the formation of this phase is from high temperatures and large plastic deformation on the rail head as a consequence of repeated loading, the specific

conditions in which they form are predicted through numerical simulations [62]. These conclusions then leave a question for what other conditions or failure mechanisms are involved to develop the white etched layer on rail head, such as events that occur during dynamic loading. This is probed here.

Previously studies involving rail steel that have focused on dynamic property measurements have found that the strength of the material increases for increasing strain rate [43] in relation to published manufacturer specifications performed at quasi-static strain rates, but little work has been completed to study the difference directly through comparing the quasi-static and dynamic loading of rail steel. Other works include [99], [102], although these studies only examined the rail wheel and tensile stress-states in quasi-static loading. Building on these past studies, this current paper focuses on the comparison of quasi-static and dynamic responses for rail steel and intends to provide information and insight into the mechanical properties and failure behaviour at elevated strain rates. From studies performed outside the rail community on steels, it is seen that the production of localizations (e.g. shears bands) are apparent in the high strain rate regimes [11, 14], which is the failure mechanism that is focused on in this work. Additionally, due to the rail steels often having a higher hardness and the higher propensity for localization formation, this work intends to provide additional insight into the long studied problem in the context of rail steel. This is completed through using high speed imaging to capture the surface of the rail steel in quasi-static and dynamic test conditions. Results are discussed in the context of our understanding of failure of steels and how this can be important for improving the performance of railway steels.

4.2 Methodology

4.2.1 Railway Material

The rail steels in this study are American Railway Engineering and Maintenance-of-Way Association (AREMA) 115 lb/yard (115 RE) and 136 lb/yard (136 RE) supplied by the Canadian National Railway Company (CN). The rail was

received in one foot sections in new condition. The rail densities used in this work are commonly used in Canadian rail transport, with lower density rails being used in secondary or low usage lines. The specimens presented in this paper were all taken at a distance of 12.7 mm from the top and side of the rail head as suggested and used by rail manufacturers following AREMA [27].

Following the current standards in place by AREMA and to remain consistent with comparison to manufacturers, Brinell hardness tests were performed on the rail head for categorizing the as-received rail steels. The Brinell hardness tests were performed with a load of 3000 kg_f and a 10 mm ball diameter indenter following the guidelines provided in ASTM E10 [103]. The tests were performed on the side face of the rail head after removing the decarburized layer. The Brinell hardness tests provide a measure of the strength of the rail, and also removes the inaccuracies of conversion between hardness systems and allows for repeatability from the use of applicable standards. For these materials, the 115 lb/yd rail had a 388 HBW and the 136 lb/yd rail had a hardness of 341 HBW.

4.2.2 Quasi-static Testing

The quasi-static compression tests were performed on rectangular specimens measuring 5.00 mm × 4.00 mm × 3.50 mm in size, using a MTS 810 testing machine. The compression specimens were made in accordance with American Society for Testing and Materials (ASTM) standards, namely ASTM 09 [104]. These tests were conducted at a strain rate of $10^{-3}\,s^{-1}$ using displacement control. The surface of the specimen was recorded using a PROMON one megapixel camera with a macro lens at a frame rate of 100 frames per second, matching the 100 Hz sampling rate of the MTS machine. The PROMON camera captured the surface of the specimen with the applied speckle pattern for use with VIC2D commercial Digital Image Correlation (DIC) software. The strain captured from the DIC software was matched with the force and displacement data recorded from the MTS machine. These data sets were matched through a physical event included in the loading procedure of the

machine. The event used was a sharp and distinct unload that was captured in both data sets. Using DIC, both small strains, large plastic strains and strain gradients can be resolved, providing accurate measurements without the need to apply compliance corrections for the universal testing machine [87]. These measurements can provide further analysis into the local and global Poisson's ratio, stress equilibrium in the sample, and quantitative data on localizations that may occur on the surface. The DIC data and the compliance corrected data was compared and were in agreement for our tests, providing additional validation for the non-contact measurement technique.

4.2.3 Split-Hopkinson Pressure Bar Testing

The dynamic compression tests of the rail material were performed with a Split-Hopkinson Pressure Bar (SHPB) apparatus. The apparatus consisted of 12.7 mm diameter Maraging C350 steel bars with a minimum hardness of 52 Rc. The bars consisted of a 304 mm striker, 914.4 mm incident bar and a 1016 mm transmission bar. The same specimen sizes were used in the dynamic experiments as the quasi-static experiments.

The SHPB is an apparatus that takes an input from a striker that is fired from a gas gun. The striker then impacts a pulse shaper that is attached to the incident bar. The use of a pulse shaper allows different loading profiles to be used to achieve proper stress equilibrium and constant strain rate in the specimen [81]. The pulse shaper used in our experiments was a mild steel with a diameter of 6.35 mm and a thickness of 0.635 mm, which follows previous studies on improving stress equilibrium and reducing the Pochhammer-Chree dispersion [88]. The specimen and the pulse shaper are both placed with a small amount of high pressure grease to reduce friction between the interfaces [81]. Additionally, the specimens length was minimized in relation to the effective radius to reduce inertial effects according to the optimal length-to-radius ratio of $\frac{\sqrt{3}}{4}$ found by Samanta [105]. These steps were performed to adhere more closely to the assumptions made in the generation of the equations seen in Equations (4.1) to (4.3).

The impact of the striker into the incident bar generates a wave in the bar that propagates to the specimen. The wave travels through the specimen and into the transmission bar where it is again recorded by a strain gauge. The signal that is captured is analyzed through using 1D wave equations. In these equations we assume no dispersion, frictional and inertial effects. The equations used for analysis are as follows [81]:

$$\dot{\varepsilon}_s = -2\frac{C_B}{L_s}\varepsilon_r \tag{4.1}$$

$$\varepsilon_s = -2\frac{C_B}{L_s}\int_0^t \varepsilon_r \, \mathrm{d}t \tag{4.2}$$

$$\sigma_s = \frac{A_B}{A_s}E_B\varepsilon_T \tag{4.3}$$

In Equations (4.1) to (4.3), $\dot{\varepsilon}_s$ is the strain rate in the specimen (s^{-1}), C_B is elastic wave speed in the incident and transmission bars ($\mathrm{m\,s}^{-1}$), L_s is the length of the specimen (m), and E_B is the elastic modulus of the bar (GPa). The area, A, and the strain calculated from the voltage signal, ε, follow the subscripts of r for the reflected wave, T for the transmitted wave, s for the specimen, and B for the bars. Stress equilibrium is achieved through obtaining a constant strain rate and this is often achieved through proper specimen design and pulse shaping. Verification of stress equilibrium is performed through a force balance, which is found and in agreement for our tests.

In all of the tests, the surface of the specimen deformation is recorded during dynamic testing using a Shimadzu HPV-X2 with an HBM GEN3i data acquisition system recording at 20 MHz. The data acquisition triggers the camera through the use of the incident pulse and is recorded in the processed data set. The camera records 128 frames at 2 million frames per second with a resolution of (400×250) pixels. At this frame rate and resolution, we are able to visualize deformation in these materials that have not yet been previously observed.

4.3 Results

In this paper, we explore the effects of strain-rate on the compressive strain-strain response and failure of two railway steels with rail weights of 115 lb/yd and 136 lb/yd. The stress-strain results obtained from the MTS 810 machine and the Split Hopkinson Pressure Bar experiments for 115 lb/yd and 136 lb/yd material are plotted in Figure 4.1. In the quasi-static compression tests, the yield strength is calculated using the 0.2% offset method due to the smooth transition into plastic deformation.

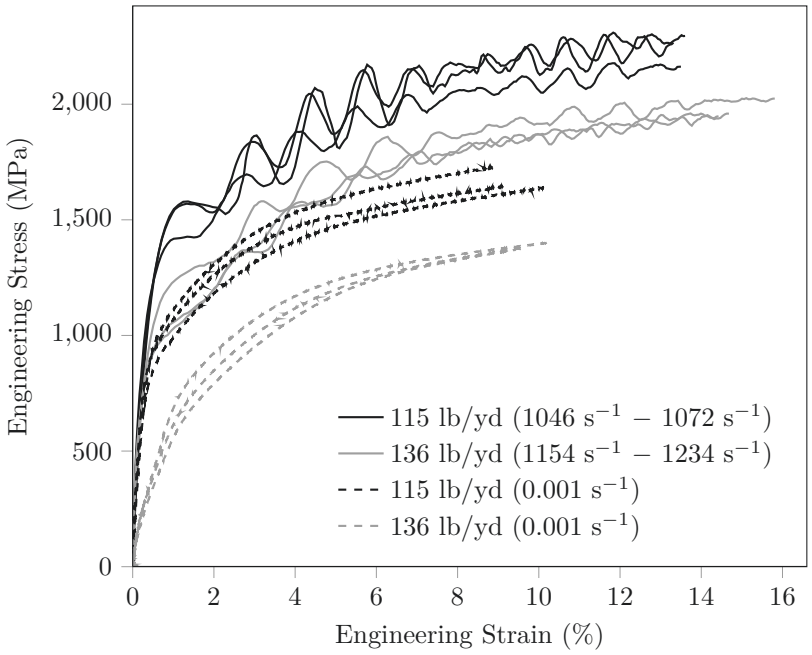

Figure 4.1. Quasi-static and dynamic compression tests performed on the 115 lb/yd and 136 lb/yd rail steels. The range denotes the tests minimum and maximum strain rates.

This method is chosen for the quasi-static case due to there being no existence of a sharp knee or a drop in load to signify yielding [104]. From the three tests that are performed for the quasi-static strain rate, the average yield strength of the 115 lb/yd rail was (934 ± 71) MPa with the resulting yield strain being (0.57 ± 0.05) %. Similarly, for the 136 lb/yd rail, the average yield strength was (623 ± 56) MPa with a yield strain of (1.01 ± 0.07) %. In Figure 4.1, these rail steels can be seen to be strain-rate dependent as there is an increase in the flow stress when the strain rate is increased. The yield strength of the 115 lb/yd rail at a average strain rate across the tests of approximately $1062\,\mathrm{s}^{-1}$ is (1528 ± 86) MPa with a yield strain of (1.28 ± 0.04) %. For the 136 lb/yd rail steel at a strain rate of $1199\,\mathrm{s}^{-1}$, a yield strength of (925 ± 67) MPa at a strain of (0.43 ± 0.03) % is reported. A summary of the yield strength and yield strain for the rail steels at both strain rates can be found in Table 4.1.

Table 4.1. The quasi-static and dynamic material characteristics for 115 lb/yd and 136 lb/yd rail steel at the respective average strain rate across all tests

	Yield Strain (%)	Yield Strength (MPa)
115 lb/yd ($10^{-3}\,\mathrm{s}^{-1}$)	0.57 ± 0.05	934 ± 71
115 lb/yd ($1062\,\mathrm{s}^{-1}$)	1.28 ± 0.04	1529 ± 86
136 lb/yd ($10^{-3}\,\mathrm{s}^{-1}$)	1.01 ± 0.07	623 ± 56
136 lb/yd ($1199\,\mathrm{s}^{-1}$)	0.43 ± 0.03	925 ± 67

Flow stress provides a measure of plastic deformation characteristics of a material, which is calculated for both the dynamic and quasi-static loading cases in this paper and is represented by:

$$\sigma_f = K\epsilon^n \tag{4.4}$$

In this equation, K is the strength coefficient (MPa), σ_f is the true flow stress (MPa), ϵ is the true strain (mm/mm), and n is the strain hardening coefficient (unitless). Through using the true stress and true strain data, the strain hardening and strength coefficient were calculated for Equation (4.4). The quasi-static strain hardening coefficient was found to be 0.25 ± 0.01 and 0.27 ± 0.02 with a strength coefficient of (3339 ± 140) MPa and (2866 ± 152) MPa for the 115 lb/yd and 136 lb/yd rail, respectively. In the high strain rate case, the

strain hardening coefficient were found to be 0.23 ± 0.01 with a strength coefficient of (4048 ± 177) MPa, and 0.24 ± 0.01 with a strength coefficient of (3649 ± 35) MPa for the 115 lb/yd and 136 lb/yd, respectively. The summary of these coefficients are shown in Table 4.2.

Table 4.2. The quasi-static and dynamic flow stress coefficient as calculated from the true stress-true strain curves

	K (MPa)	n
115 lb/yd ($10^{-3}\,s^{-1}$)	3339 ± 140	0.25 ± 0.01
115 lb/yd ($1062\,s^{-1}$)	4048 ± 177	0.23 ± 0.01
136 lb/yd ($10^{-3}\,s^{-1}$)	2866 ± 152	0.27 ± 0.02
136 lb/yd ($1199\,s^{-1}$)	3649 ± 35	0.24 ± 0.01

Next, we investigate the dynamic deformation features in Figures 4.2a to 4.2c and Figures 4.2d to 4.2f is a collection of still images from dynamic tests using a ultra-high-speed camera for the 115 lb/yd and 136 lb/yd rail, respectively. The progression of surface texturing is shown with the corresponding strains in the still images. From left to right, the first images show the undeformed face of the specimen with no texturing present. The middle set of images are when the surface texturing first begins to occur. Lastly, the final images are taken at similar strains (5.1 %) to show the fully developed texturing on the rail specimens. The results from our study demonstrate that surface texturing and subsequent hardening is shown in dynamic loading. The size of the features are taken as circular and the diameters are found to be similar for both the 115 lb/yd rail and the 136 lb/yd rail steel, although, from visual inspection, it seems that the surface texturing on the 136 lb/yd rail is more aggressive. Similarly, the surface texturing is seen in the quasi-static case at strains $> 1.5\%$. This suggests this surface texturing is not limited to higher strain rates. From the three tests conducted of each material using the Split-Hopkinson Pressure Bar, the texturing begins at (1.4 ± 0.3) % strain for the 115 lb/yd rail steel and (1.3 ± 0.3) % for the 136 lb/yd rail steel as measured from the high speed images at average loading rates of $(1062 \pm 14)\,s^{-1}$ and $(1199 \pm 41)\,s^{-1}$, respectively. In both materials studied here, surface texturing can occur for strains $< 2\%$ and these are of the order of (104 ± 29) µm and (109 ± 26) µm in size for the

115 lb/yd and 136 lb/yd, respectively. As the surface is strained further, the texturing becomes more defined. In Figure 4.2, surface texturing is found at approximately the same strain that yield onset occurs when comparing the SHPB strain data to the visually captured images and resulting strain. From this, we attribute the softening behaviour in dynamic loading to the strain localizations seen through the surface texturing.

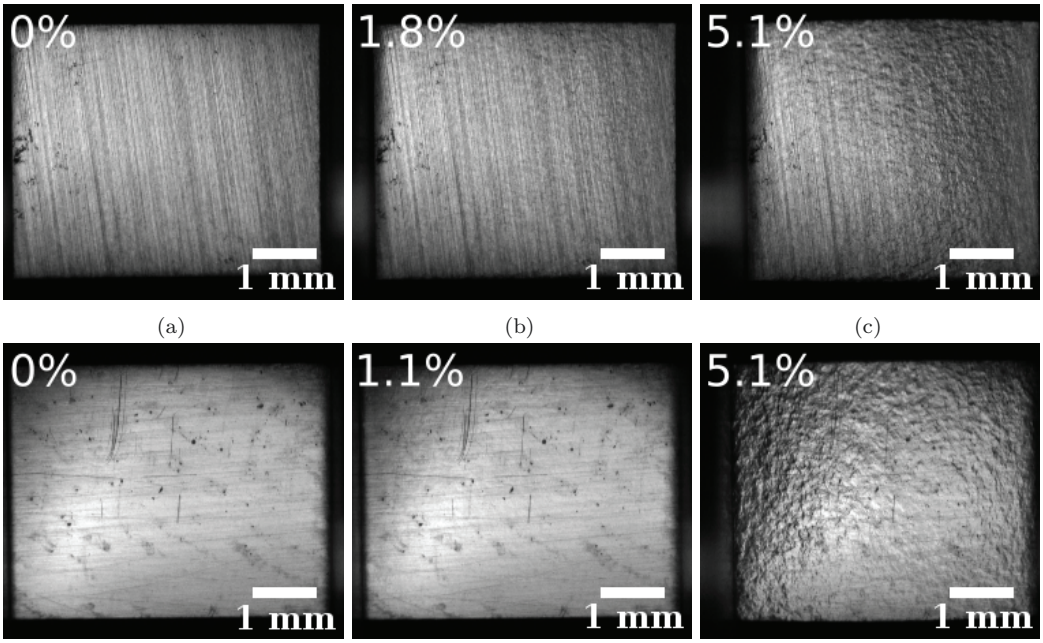

Figure 4.2. Surface images recorded at 2 million frames per second using the Shimadzu HPVX-2 of 115 lb/yd ($\dot{\bar{\varepsilon}} = 1062\,\mathrm{s}^{-1}$): (a) underformed specimen, (b) start of surface texturing begins at a strain of 1.8 % and, (c) surface texturing when fully developed on the face of the specimen at a strain of 5.1 %. 136 lb/yd at an average rate of $\dot{\bar{\varepsilon}} = 1199\,\mathrm{s}^{-1}$: (d) underformed, (e) start of surface texturing begins at a strain of 1.1 % and, (f) surface texturing when fully developed on the face of the specimen at a strain of 5.1 %

4.4 Discussion

From our tests, we have found that 115 lb/yd rail has a higher yield strength than 136 lb/yd rail in both the dynamic and quasi-static testing. Finding the flow stress coefficients shows that the strain hardening is not strain rate dependent while the strength coefficient is. The surface feature size and the strain at which surface texturing begins is similar for both materials (between

1% to 2%), and these localizations are related to softening in the stress-strain responses of the rail steels. Overall, the stress-strain measurements contribute to a limited data set in the literature on the rate-dependent mechanical properties of steels used in railway (e.g. compression [8, 43] and tension [99]). The magnitudes of the strengths and behaviours are found to be similar ($> 1\,\text{GPa}$) as those reported by Nakkalil *et al.* (1991) for other commonly used rail steels and for Jing *et al.* (2016) steel used in the rail wheels, although different specimen sizes, uncertainty, and experimental setups are noted. In our study, a change in yield behaviour for the 115 lb/yd rail is found when strain rates are increased, changing from a gradual transition into plastic deformation to a sharp-kneed yield point. The change in yield behaviour was observed to be a consequence of dynamic failure mechanisms being activated in high strain rate loading and increased thermal softening. In a separate study on the rate-dependent tensile response of rail wheel steel by Jing *et al.* (2016), a rate-dependency was seen for the mechanical properties in tension and softening occurred at the onset of plastic deformation. Jing *et al.* (2016) attributed both trends to an increase in ductility for the higher strain rates. Here, again, we associate the changes in the stress-strain curves with the onset and evolution of texturing, which is more pronounced for higher strain rates. Next, we connect our mechanical property and failure mechanism results to our current understanding of failure of the rail.

In the literature, spheroidized pearlite is commonly observed on the surface of rail along with large deformations at these sites [56, 58]. This spheroidized pearlite and martensite often makes up the White Etched Layer (WEL) on the rail, which is found to be a precursor to rail fracture [59, 106]. Wu *et al.* (2016) summarizes two main processes that are thought to form WEL, 1. martensitic transformation by heat generation, and 2. extreme plastic deformation. In a numerical study by Ertz and Knothe (2002), the temperature rise on the head of the rail was observed to not be sufficient enough to product the WEL alone, even though martensite is often present in real conditions. In another numerical study, the temperature rise was seen to become sufficient enough

to form the martensite through increasing the roughness on the surface of the rail [56]. This condition gives rise to the possibility of the texturing found in this paper to exist in real world conditions. Further, it is found that for laboratory generation of the WEL is possible, but is not exactly similar to that found on used rail [56]. In laboratory-created WEL, the hardness is found to be lower, average grain sizes are smaller and more austenite is found in comparison with the WEL from literature and real world applications [56]. This suggests that while multiple conditions must exist simultaneously, there are interactions between these separate mechanisms to produce WEL. To link these concepts back to our results, our results indicate that through the combination of specific processes the generation of WEL may not independently require large strains, plastic deformation, and significant heating to produce hardened spherical features on the surface rail. Instead, we have shown that strains $< 2\%$ in compression and dynamic strain rate regimes, promote the initiation and growth of small local features that may aid in heat generation and the required plastic deformation on the surface. These rates and stresses are entirely achievable in rail applications with the most extreme cases occurring at crossings and joints [107]. Further, repeated loading from rails likely results in additional surface texturing and subsequent increased heat generation on textured surfaces, and this further contributes to hardening and generation of the WEL. Altogether, our work motivates the need to study dynamic behavior of rail steel so that we can design improved materials in the future.

4.5 Conclusion

This paper investigated the strain rate dependent compressive response of 115 lb/yd and 136 lb/yd rail steel, focusing on the links between failure and the stress-strain responses. The 115 lb/yd rail had a yield strength in quasi-static conditions of (934 ± 71) MPa, while in dynamic loading it had a yield strength of (1528 ± 86) MPa. The 136 lb/yd rail had a yield strength of (623 ± 56) MPa and (925 ± 67) MPa in quasi-static and dynamic loading, respectively. For both

materials, the strain hardening was found to be similar and remained constant between the quasi-static and dynamic strain rates. Both steels exhibited surface texturing in dynamic loading with similar size textures with the texturing approximately occurring around the yield of the material. This mechanism is believe to correspond with the development of the WEL on rail steels.

4.6 Acknowledgments

This work was sponsored by the Canadian Rail Research Laboratory (CaRRL). CaRRL receives funding from the Natural Sciences and Engineering Research Council of Canada (NSERC), Canadian Pacific Railway, Canadian National Railway, the Association of American Railways – Transportation Technology Centre Inc., Transport Canada and Alberta Innovates.

Chapter 5

Conclusion

5.1 Summary

In this thesis, the dynamic failure of rail and naval steels has been explored. Comparing the naval and rail steels, it was seen that the naval steel had a much higher strain hardening coefficient than the rail steels examined in the thesis. All steels examined were found to be strain rate sensitive, the yield strengths and flow stresses were increased with increasing strain rate. The in-situ imaging of these experiments has provided insight on the nucleation and propagation of shear bands in quasi-static and dynamic compression. It has provided insight of the nucleation location, direction and velocity of the shear bands as seen on the surface of the specimens for the HSLA 65 naval steel. The texturing found for the rail steels supports the theories developed in context of the white etching layer and suggests the processes, which occur in the development of the white etching layer and shear bands.

In summary,

- Chapter 1 provides motivation for studying shear bands for improving materials used in many industries. These industries gain large investment for developing new technologies to improve the performance and safety of ships and rail transportation.
- Chapter 2 explores a literature review of the current understanding of shear bands and the white etching layer. This includes the processes that

are expected in their development, the identification of this phenomena, and the implications they have on material stability. Similarly, the white etching layer is explored in relation to their development with shear bands. Included in this chapter is a brief overview of the testing techniques and the materials tested in this thesis.

- Chapter 3 is a work on observing shear bands in HSLA 65, a naval steel used in North America, and providing information on the shear bands velocity. This work also includes quasi-static and dynamic stress-strain information on HSLA 65, in which the shear bands formation is compared. This work provides shear band velocity in a relatively simple stress-state that can be modelled and subsequently compared.

- Chapter 4 focuses on the formation of the WEL and provides information on the development of this layer. This is completed by observing the in-situ behaviour of the deformation of commonly used rail steels in Canada at time scales not available, to my knowledge, in the literature. Similarly, the stress-strain responses of the rail steels are provided.

5.2 Implications

The objective of this thesis was to examine and provide context on the length scales and time scales that the shear band and WEL localizations occur. In this thesis, data and perspective has been generated for both localizations such as shear bands and the WEL that form in high strain-rate conditions. The work has provided an experimental setup and materials that can be studied further for the localizations that occur. First, compressive quasi-static and dynamic material response, which are more representative of operation conditions, have been shown and discussed in relation to commonly occurring WEL and shear band localizations providing valuable insight of materials that are commonly used, but lack extensive characterization in the literature. This collected data is then coupled with the characterization of propagation velocity, orientation of formation and strains at which these occur for shear banding. In

the context of the rail industry, the behaviour of the steel is coupled with the beginning formation strain, texturing characteristics such as the diameter of the surface texturing, and progression of formation of the surface texturing over the duration of the test. The implications of this work include insights on the formation velocities, strain and time scales, which is valuable for further research on the conditions the localizations form. The velocity and nucleation strains of shear bands aid in the study of nucleation and instability modelling with relatively simple stress-state experimental data for validation. The information and perspectives of the shear banding and WEL localization phenomena shown here provide insight on developing new materials as specific alloying, heat treating and microstructure may be the governing factors of these visible bands. Lastly, the formation of visible shear banding aids in material selection that dictate the failure behaviour and material behaviour of steels used in rail and naval applications, and in general, the ability to make more informed decisions on material selection in high strain rate applications.

5.3 Future Work

- Quantify shear band characteristics such as strain field, strain rate and propagation with Digital Image Correlation for quasi-static and dynamic compressive loading. This would further develop the information provided in this thesis for use in validating models to obtain higher quality predictions. These models further could be used to study different loading conditions and strain rates.

- Analyze the formed surface texturing of the rail steel with methods such as Scanning Electron Microscopy (SEM), X-Ray Diffraction (XRD), Electron Backscatter Diffraction (EBSD), and nano-indentation. This information would allow for better understanding of how the surface texturing impacts the development of the white etched layer, shear bands and crack propagation. For example, how is the characteristics of this texturing related to increased heat generation or plastic deformation.

References

[1] A. Johansson and J. C. O. Nielsen, "Out-of-round railway wheels—wheel-rail contact forces and track response derived from field tests and numerical simulations," *Proceedings of the Institution of Mechanical Engineers, Part F: Journal of Rail and Rapid Transit*, vol. 217, no. 2, pp. 135–146, Mar. 2003, ISSN: 0954-4097, 2041-3017. DOI: 10.1243/095440903765762878.

[2] A. A. Tiamiyu, V. Tari, J. A. Szpunar, A. G. Odeshi, and A. K. Khan, "Effects of grain refinement on the quasi-static compressive behavior of AISI 321 austenitic stainless steel: EBSD, TEM, and XRD studies," *International Journal of Plasticity*, vol. 107, pp. 79–99, Aug. 1, 2018, ISSN: 0749-6419. DOI: 10.1016/j.ijplas.2018.03.014.

[3] J. Johansson, C. Persson, G. Testa, A. Ruggiero, N. Bonora, and M. Hörnqvist Colliander, "Effect of microstructure on dynamic shear localisation in Alloy 718," *Mechanics of Materials*, vol. 109, pp. 88–100, Jun. 2017, ISSN: 01676636. DOI: 10.1016/j.mechmat.2017.03.020.

[4] C. McVeigh and W. K. Liu, "Linking microstructure and properties through a predictive multiresolution continuum," *Computer Methods in Applied Mechanics and Engineering*, vol. 197, no. 41-42, pp. 3268–3290, Jul. 2008, ISSN: 00457825. DOI: 10.1016/j.cma.2007.12.020.

[5] Statistics Canada. (May 13, 2019). Table 23-10-0051-01 Railway industry length of track operated at the end of the year, by company, [Online]. Available: https://www150-statcan-gc-ca.login.ezproxy.library.ualberta.ca/t1/tbl1/en/tv.action?pid=2310005101 (visited on 05/13/2019).

[6] ——, (May 13, 2019). Table 23-10-0216-01 Railway carloadings statistics, by commodity, by region, monthly, [Online]. Available: https://www150-statcan-gc-ca.login.ezproxy.library.ualberta.ca/t1/tbl1/en/cv.action?pid=2310021601#timeframe (visited on 05/13/2019).

[7] P. S. a. P. C. Government of Canada. (Jun. 8, 2018). Shipbuilding projects to equip the Royal Canadian Navy and the Canadian Coast Guard – National Shipbuilding Strategy – Sea – Defence Procurement – Buying and Selling – PSPC, [Online]. Available: https://www.tpsgc-pwgsc.gc.ca/app-acq/amd-dp/mer-sea/sncn-nss/projets-projects-eng.html#s1 (visited on 05/13/2019).

[8] R. Nakkalil, "Formation of adiabatic shear bands in eutectoid steels in high strain rate compression," *Acta Metallurgica et Materialia*, vol. 39, no. 11, pp. 2553–2563, Nov. 1, 1991, ISSN: 0956-7151. DOI: 10.1016/0956-7151(91)90070-H.

[9] A. Marchand and J. Duffy, "An experimental study of the formation process of adiabatic shear bands in a structural steel," *Journal of the Mechanics and Physics of Solids*, vol. 36, no. 3, pp. 251–283, Jan. 1, 1988, ISSN: 0022-5096. DOI: 10.1016/0022-5096(88)90012-9.

[10] O. Oussouaddi, L. Daridon, S. Ahzi, and A. Chrysochoos, "Influence of dissipated energy on shear band spacing in HY-100 steel," *Journal of Engineering Materials and Technology*, vol. 133, no. 2, p. 021 002, 2011.

[11] G. Owolabi, D. Odoh, A. Odeshi, and H. Whitworth, "Occurrence of Dynamic Shear Bands in AISI 4340 Steel under Impact Loads," *World Journal of Mechanics*, vol. 03, no. 02, pp. 139–145, 2013, ISSN: 2160-049X, 2160-0503. DOI: 10.4236/wjm.2013.32011.

[12] W. W. Du, Q. Wang, D. H. Zhao, and L. Wang, "Study on the Evolution of Adiabatic Shear Band of a High Strength Steel," *Applied Mechanics and Materials*, vol. 782, pp. 143–150, Aug. 2015, ISSN: 1662-7482. DOI: 10.4028/www.scientific.net/AMM.782.143.

[13] C. K. Syn, D. R. Lesuer, and O. D. Sherby, "Microstructure in adiabatic shear bands in a pearlitic ultrahigh carbon steel," *Materials science and technology*, vol. 21, no. 3, pp. 317–324, 2005.

[14] I. Mendoza, D. Villalobos, and B. Alexandrov, "Crack propagation of Ti alloy via adiabatic shear bands," *Materials Science and Engineering: A*, vol. 645, pp. 306–310, Oct. 2015, ISSN: 09215093. DOI: 10.1016/j.msea.2015.08.035.

[15] Y. Xu, Y. Bai, Q. Xue, and L. Shen, "Formation, microstructure and development of the localized shear deformation in low-carbon steels," *Acta Materialia*, vol. 44, no. 5, pp. 1917–1926, May 1, 1996, ISSN: 1359-6454. DOI: 10.1016/1359-6454(95)00306-1.

[16] D. Odoh, G. Owolabi, A. Odeshi, and H. Whitworth, "Shear band formation in AISI 4340 steel under dynamic impact loads: Modeling and experiment," *Acta Metallurgica Sinica (English Letters)*, vol. 26, no. 4, pp. 378–384, Aug. 2013, ISSN: 1006-7191, 2194-1289. DOI: 10.1007/s40195-013-0103-2.

[17] G. M. Swallowe, "Adiabatic Shear Bands in Polymers," in *Adiabatic Shear Localization*, Elsevier, 2012, pp. 363–398, ISBN: 978-0-08-097781-2. DOI: 10.1016/B978-0-08-097781-2.00009-5.

[18] Fakhimi A., Riedel J. J., and Labuz J. F., "Shear Banding in Sandstone: Physical and Numerical Studies," *International Journal of Geomechanics*, vol. 6, no. 3, pp. 185–194, May 1, 2006. DOI: 10.1061/(ASCE)1532-3641(2006)6:3(185).

[19] M. S. Rashid, "High-Strength, Low-Alloy Steels," *Science*, vol. 208, no. 4446, pp. 862–869, May 23, 1980, ISSN: 0036-8075, 1095-9203. DOI: 10.1126/science.208.4446.862.

[20] A01 Committee, "Specification for High-Strength Low-Alloy Structural Steel," ASTM International. DOI: 10.1520/A0242_A0242M-13R18.

[21] J. R. Davis, Ed., *Alloying: Understanding the Basics*, Materials Park, OH: ASM International, 2001, 647 pp., ISBN: 978-0-87170-744-4.

[22] T. W. Montemarano, B. P. Sack, J. P. Gudas, M. G. Vassilaros, and H. H. Vanderveldt, "High Strength Low Alloy Steels in Naval Construction," *Journal of Ship Production*, vol. 2, no. 3, pp. 145–162, Aug. 1986.

[23] A01 Committee, "Specification for High-Strength Low-Alloy Structural Steel Plate with Low Carbon and Restricted Sulfur for Improved Weldability, Formability, and Toughness," ASTM International. DOI: 10.1520/A0945_A0945M-16.

[24] S. R. Heller, I. Fioriti, and J. Vasta, "AN EVALUATION OF HY-80 STEEL AS A STRUCTURAL MATERIAL FOR SUBMARINES," *Naval Engineers Journal*, vol. 77, no. 1, pp. 29–44, Feb. 1965, ISSN: 00281425, 15593584. DOI: 10.1111/j.1559-3584.1965.tb05644.x.

[25] ——, "An Evaluation of Hy-80 Steel. as a Structural Material for Submarines. Part Ii," *Naval Engineers Journal*, vol. 77, no. 2, pp. 193–200, 1965, ISSN: 1559-3584. DOI: 10.1111/j.1559-3584.1965.tb05346.x.

[26] K. Sawley and J. Kristan, "Development of bainitic rail steels with potential resistance to rolling contact fatigue," *Fatigue & Fracture of Engineering Materials & Structures*, vol. 26, no. 10, pp. 1019–1029, Oct. 2003, ISSN: 8756-758X, 1460-2695. DOI: 10.1046/j.1460-2695.2003.00671.x.

[27] A. R. Engineering and M.-W. Association, "Manual for railway engineering," 2017, Description based on: 1999, ISSN: 1542-8036.

[28] R. Ordonez, C. Garcia, A. Deardo, and S. Kalay, "New rail steels for the 21st century," *Materials Science and Technology Conference and Exhibition 2009, MS and T'09*, vol. 3, pp. 1614–1624, Jan. 1, 2009.

[29] W. Lojkowski, M. Djahanbakhsh, G. Bürkle, S. Gierlotka, W. Zielinski, and H.-J. Fecht, "Nanostructure formation on the surface of railway tracks," *Materials Science and Engineering: A*, vol. 303, no. 1-2, pp. 197–208, May 2001, ISSN: 09215093. DOI: 10.1016/S0921-5093(00)01947-X.

[30] D. Szablewski and J. LoPresti, "Development and Evaluation of High Performance Rail Steels for Heavy Haul Operations," p. 10,

[31] M. A. Meyers, V. F. Nesterenko, J. C. LaSalvia, and Q. Xue, "Shear localization in dynamic deformation of materials: Microstructural evolution and self-organization," *Materials Science and Engineering: A*, vol. 317, no. 1, pp. 204–225, Oct. 31, 2001, ISSN: 0921-5093. DOI: 10.1016/S0921-5093(01)01160-1.

[32] P. R. Guduru, A. J. Rosakis, and G. Ravichandran, "Dynamic shear bands: An investigation using high speed optical and infrared diagnostics," *Mechanics of Materials*, vol. 33, no. 7, pp. 371–402, Jul. 1, 2001, ISSN: 0167-6636. DOI: 10.1016/S0167-6636(01)00051-5.

[33] S. Thuillier and E. Rauch, "Development of microbands in mild steel during cross loading," *Acta Metallurgica et Materialia*, vol. 42, no. 6, pp. 1973–1983, Jun. 1994, ISSN: 09567151. DOI: 10.1016/0956-7151(94)90022-1.

[34] L. F. Liu, L. H. Dai, Y. L. Bai, and B. C. Wei, "Initiation and propagation of shear bands in Zr-based bulk metallic glass under quasi-static and dynamic shear loadings," *Journal of Non-Crystalline Solids*, vol. 351, no. 40, pp. 3259–3270, Oct. 15, 2005, ISSN: 0022-3093. DOI: 10.1016/j.jnoncrysol.2005.07.030.

[35] M. Zhou, A. J. Rosakis, and G. Ravichandran, "Dynamically propagating shear bands in impact-loaded prenotched plates—I. Experimental investigations of temperature signatures and propagation speed," *Journal of the Mechanics and Physics of Solids*, vol. 44, no. 6, pp. 981–1006, 1996.

[36] T. W. Wright and R. C. Batra, "The initiation and growth of adiabatic shear bands," *International Journal of Plasticity*, vol. 1, no. 3, pp. 205–212, 1985.

[37] M. Arriaga, C. McAuliffe, and H. Waisman, "Instability analysis of shear bands using the instantaneous growth-rate method," *International Journal of Impact Engineering*, vol. 87, pp. 156–168, Jan. 2016, ISSN: 0734743X. DOI: 10.1016/j.ijimpeng.2015.04.004.

[38] I. Polyzois and N. Bassim, "Microstructural simulation of adiabatic shear band formation in AISI 4340 steel using Voronoi Tessellation," *Computational Materials Science*, vol. 109, pp. 157–171, Nov. 2015, ISSN: 09270256. DOI: 10.1016/j.commatsci.2015.06.041.

[39] S. Nemat-Nasser and W.-G. Guo, "Thermomechanical response of HSLA-65 steel plates: Experiments and modeling," *Mechanics of Materials*, vol. 37, no. 2-3, pp. 379–405, Feb. 2005, ISSN: 01676636. DOI: 10.1016/j.mechmat.2003.08.017.

[40] M. Liu, Z. Guo, C. Fan, T. Tang, X. Wang, and H. Hu, "Modeling spontaneous shear bands evolution in thick-walled cylinders subjected to external High-strain-rate loading," *International Journal of Solids and Structures*, vol. 97-98, pp. 336–354, Oct. 2016, ISSN: 00207683. DOI: 10.1016/j.ijsolstr.2016.07.014.

[41] N. Jia, P. Eisenlohr, F. Roters, D. Raabe, and X. Zhao, "Orientation dependence of shear banding in face-centered-cubic single crystals," *Acta Materialia*, vol. 60, no. 8, pp. 3415–3434, May 2012, ISSN: 13596454. DOI: 10.1016/j.actamat.2012.03.005.

[42] S. Nemat-Nasser and W.-G. Guo, "Thermomechanical response of DH-36 structural steel over a wide range of strain rates and temperatures," *Mechanics of Materials*, vol. 35, no. 11, pp. 1023–1047, Nov. 1, 2003, ISSN: 0167-6636. DOI: 10.1016/S0167-6636(02)00323-X.

[43] R. Nakkalil, J. R. Hornaday, and M. N. Bassim, "Characterization of the compression properties of rail steels at high temperatures and strain rates," *Materials Science and Engineering: A*, vol. 141, no. 2, pp. 247–260, 1991.

[44] V. Pushkov, A. Yurlov, A. Bol'shakov, A. Podurets, A. Kal'manov, and E. Koshatova, "Study of adiabatic localized shear in metals by split Hopkinson pressure bar method," *EPJ Web of Conferences*, vol. 10, p. 00 029, 2010, ISSN: 2100-014X. DOI: 10.1051/epjconf/20101000029.

[45] R. Batra and D.-S. Liu, "Adiabatic shear banding in dynamic plane strain compression of a viscoplastic material," *International Journal of Plasticity*, vol. 6, no. 2, pp. 231–246, Jan. 1990, ISSN: 07496419. DOI: 10.1016/0749-6419(90)90023-8.

[46] B. Zhang, Y. Liu, W. Shen, Y. Wang, X. Tang, and X. Wang, "A study on the behavior of adiabatic shear bands in impact wear," *Wear*, vol. 198, no. 1-2, pp. 287–292, Oct. 1996, ISSN: 00431648. DOI: 10.1016/0043-1648(96)07209-2.

[47] G. Owolabi, D. Bolling, A. Tiamiyu, R. Abu, A. Odeshi, and H. Whitworth, "Shear strain localization in AA 2219-T8 aluminum alloy at high strain rates," *Materials Science and Engineering: A*, vol. 655, pp. 212–220, Feb. 2016, ISSN: 09215093. DOI: 10.1016/j.msea.2015.12.100.

[48] J. A. Hines and K. S. Vecchio, "Recrystallization kinetics within adiabatic shear bands," *Acta Materialia*, vol. 45, no. 2, pp. 635–649, Feb. 1, 1997, ISSN: 1359-6454. DOI: 10.1016/S1359-6454(96)00193-0.

[49] J. Johansson, C. Persson, H. Lai, and M. Hörnqvist Colliander, "Microstructural examination of shear localisation during high strain rate deformation of Alloy 718," *Materials Science and Engineering: A*, vol. 662, pp. 363–372, Apr. 2016, ISSN: 09215093. DOI: 10.1016/j.msea.2016.03.080.

[50] M. Meyers, Y. Xu, Q. Xue, M. Pérez-Prado, and T. McNelley, "Microstructural evolution in adiabatic shear localization in stainless steel," *Acta Materialia*, vol. 51, no. 5, pp. 1307–1325, Mar. 2003, ISSN: 13596454. DOI: 10.1016/S1359-6454(02)00526-8.

[51] H. Yang, Y. Xu, Y. Seki, V. F. Nesterenko, and M. A. Meyers, "Analysis and characterization by electron backscatter diffraction of microstructural evolution in the adiabatic shear bands in Fe–Cr–Ni alloys," *Journal of Materials Research*, vol. 24, no. 8, pp. 2617–2627, Aug. 2009, ISSN: 0884-2914, 2044-5326. DOI: 10.1557/jmr.2009.0322.

[52] A. Odeshi, S. Al-ameeri, S. Mirfakhraei, F. Yazdani, and M. Bassim, "Deformation and failure mechanism in AISI 4340 steel under ballistic impact," *Theoretical and Applied Fracture Mechanics*, vol. 45, no. 1, pp. 18–24, Feb. 2006, ISSN: 01678442. DOI: 10.1016/j.tafmec.2005.11.005.

[53] X. Chen, Q. Li, and S. Fan, "Initiation of adiabatic shear failure in a clamped circular plate struck by a blunt projectile," *International Journal of Impact Engineering*, vol. 31, no. 7, pp. 877–893, Aug. 2005, ISSN: 0734743X. DOI: 10.1016/j.ijimpeng.2004.04.011.

[54] H. M. Ghomi and A. G. Odeshi, "The effects of microstructure, strain rates and geometry on dynamic impact response of a carbon–manganese steel," *Materials Science and Engineering: A*, vol. 532, pp. 308–315, Jan. 15, 2012, ISSN: 0921-5093. DOI: 10.1016/j.msea.2011.10.096.

[55] P. N. Ryabov, N. A. Kudryashov, and R. V. Muratov, "Adiabatic shear bands localization in materials undergoing deformations," *Journal of Physics: Conference Series*, vol. 788, p. 012 031, Jan. 2017, ISSN: 1742-6588, 1742-6596. DOI: 10.1088/1742-6596/788/1/012031.

[56] J. Wu, R. H. Petrov, M. Naeimi, Z. Li, R. Dollevoet, and J. Sietsma, "Laboratory simulation of martensite formation of white etching layer in rail steel," *International Journal of Fatigue*, vol. 91, pp. 11–20, Oct. 2016, ISSN: 01421123. DOI: 10.1016/j.ijfatigue.2016.05.016.

[57] M. Neslušan, J. Čížek, K. Zgútová, P. Kejzlar, J. Šramek, J. Čapek, P. Hruška, and O. Melikhova, "Microstructural transformation of a rail surface induced by severe thermoplastic deformation and its non-destructive monitoring via Barkhausen noise," *Wear*, vol. 402-403, pp. 38–48, May 15, 2018, ISSN: 0043-1648. DOI: 10.1016/j.wear.2018.01.014.

[58] S. B. Newcomb and W. M. Stobbs, "A transmission electron microscopy study of the white-etching layer on a rail head," *Materials Science and Engineering*, vol. 66, no. 2, pp. 195–204, Sep. 15, 1984, ISSN: 0025-5416. DOI: 10.1016/0025-5416(84)90180-0.

[59] J. W. Seo, S. J. Kwon, H. K. Jun, and D. H. Lee, "Microstructure Features and Contact Fatigue Crack Growth on Rail," *Materials Science Forum*, vol. 654-656, pp. 2491–2494, Jun. 2010, ISSN: 1662-9752. DOI: 10.4028/www.scientific.net/MSF.654-656.2491.

[60] J. Takahashi, K. Kawakami, and M. Ueda, "Atom probe tomography analysis of the white etching layer in a rail track surface," *Acta Materialia*, vol. 58, no. 10, pp. 3602–3612, Jun. 1, 2010, ISSN: 1359-6454. DOI: 10.1016/j.actamat.2010.02.030.

[61] A. Kumar, G. Agarwal, R. Petrov, S. Goto, J. Sietsma, and M. Herbig, "Microstructural evolution of white and brown etching layers in pearlitic rail steels," *Acta Materialia*, vol. 171, pp. 48–64, Jun. 1, 2019, ISSN: 1359-6454. DOI: 10.1016/j.actamat.2019.04.012.

[62] M. Ertz and K. Knothe, "A comparison of analytical and numerical methods for the calculation of temperatures in wheel/rail contact," *Wear*, vol. 253, no. 3, pp. 498–508, Aug. 1, 2002, ISSN: 0043-1648. DOI: 10.1016/S0043-1648(02)00120-5.

[63] H. W. Zhang, S. Ohsaki, S. Mitao, M. Ohnuma, and K. Hono, "Microstructural investigation of white etching layer on pearlite steel rail," *Materials Science and Engineering: A*, Internal Stress and Thermo-Mechanical Behavior in Multi-Component Materials Systems, TMS Annual Meeting, 2004, vol. 421, no. 1, pp. 191–199, Apr. 15, 2006, ISSN: 0921-5093. DOI: 10.1016/j.msea.2006.01.033.

[64] R. I. Carroll and J. H. Beynon, "Rolling contact fatigue of white etching layer: Part 1 Crack morphology," p. 14, 2007.

[65] F. A. M. Alwahdi, A. Kapoor, and F. J. Franklin, "Subsurface microstructural analysis and mechanical properties of pearlitic rail steels in service," *Wear*, Wear of Materials 2013, vol. 302, no. 1, pp. 1453–1460, Apr. 1, 2013, ISSN: 0043-1648. DOI: 10.1016/j.wear.2012.12.058.

[66] J. Wu, R. H. Petrov, S. Kölling, P. Koenraad, L. Malet, S. Godet, and J. Sietsma, "Micro and Nanoscale Characterization of Complex Multilayer-Structured White Etching Layer in Rails," *Metals*, vol. 8, no. 10, p. 749, Oct. 2018. DOI: 10.3390/met8100749.

[67] O. Vargolici, P. Merino, A. Saulot, J. Cavoret, S. Simon, F. Ville, and Y. Berthier, "Influence of the initial surface state of bodies in contact on the formation of white etching layers under dry sliding conditions," *Wear*, Contact Mechanics and Wear of Rail / Wheel Systems, CM2015, August 2015, vol. 366-367, pp. 209–216, Nov. 15, 2016, ISSN: 0043-1648. DOI: 10.1016/j.wear.2016.06.023.

[68] S. Hosseini, U. Klement, Y. Yao, and K. Ryttberg, "Formation mechanisms of white layers induced by hard turning of AISI 52100 steel," *Acta Materialia*, vol. 89, pp. 258–267, May 2015, ISSN: 13596454. DOI: 10.1016/j.actamat.2015.01.075.

[69] B. Zhang, W. Shen, Y. Liu, and R. Zhang, "Some factors influencing adiabatic shear banding in impact wear," *Wear*, vol. 214, no. 2, pp. 259–263, Feb. 1, 1998, ISSN: 0043-1648. DOI: 10.1016/S0043-1648(97)00238-X.

[70] W. Wang, H. Zhang, M. Yang, P. Jiang, F. Yuan, and X. Wu, "Shock and Spall Behaviors of a High Specific Strength Steel: Effects of Impact Stress and Microstructure," *Journal of Applied Physics*, vol. 121, no. 13, p. 135 901, Apr. 7, 2017, ISSN: 0021-8979, 1089-7550. DOI: 10.1063/1.4979346.

[71] A. S. Savinykh, G. V. Garkushin, S. V. Razorenov, S. Wolf, and L. Kruger, "Influence of the temperature-induced martensitic-austenitic transformation on the strength properties of high-alloy steels under dynamic loading," *Combustion, Explosion, and Shock Waves*, vol. 51, no. 1, pp. 124–129, Jan. 2015, ISSN: 0010-5082, 1573-8345. DOI: 10.1134/S001050821501013X.

[72] G. Gray, V. Livescu, P. Rigg, C. Trujillo, C. Cady, S. Chen, J. Carpenter, T. Lienert, and S. Fensin, "Structure/Property (constitutive and Spallation Response) of Additively Manufactured 316L Stainless Steel," *Acta Materialia*, vol. 138, pp. 140–149, Oct. 2017, ISSN: 13596454. DOI: 10.1016/j.actamat.2017.07.045.

[73] R. W. Armstrong and S. M. Walley, "High strain rate properties of metals and alloys," *International Materials Reviews*, vol. 53, no. 3, pp. 105–128, May 2008, ISSN: 0950-6608, 1743-2804. DOI: 10.1179/174328008X277795.

[74] G. Majzoobi, A. Mahmoudi, and S. Moradi, "Ductile to brittle failure transition of HSLA-100 Steel at high strain rates and subzero temperatures," *Engineering Fracture Mechanics*, vol. 158, pp. 179–193, Jun. 2016, ISSN: 00137944. DOI: 10.1016/j.engfracmech.2016.03.001.

[75] N. K. Singh, E. Cadoni, M. K. Singha, and N. K. Gupta, "Quasi-Static and Dynamic Tensile Behavior of CP800 Steel," *Mechanics of Advanced Materials and Structures*, vol. 21, no. 7, pp. 531–537, Aug. 9, 2014, ISSN: 1537-6494, 1537-6532. DOI: 10.1080/15376494.2012.699594.

[76] W. Guo, J. Liu, J. Yang, and S. Li, "Effect of initial temperature on dynamic recrystallization of tungsten and matrix within adiabatic shear band of tungsten heavy alloy," *Materials Science and Engineering: A*, vol. 528, no. 19-20, pp. 6248–6252, Jul. 2011, ISSN: 09215093. DOI: 10.1016/j.msea.2011.04.080.

[77] L. W. Meyer and F. Pursche, "Experimental Methods," in *Adiabatic Shear Localization*, Elsevier, 2012, pp. 21–109, ISBN: 978-0-08-097781-2. DOI: 10.1016/B978-0-08-097781-2.00002-2.

[78] R. Panowicz, J. Janiszewski, and K. Kochanowski, "Influence of pulse shaper geometry on wave pulses in SHPB experiments," *Journal of Theoretical and Applied Mechanics*, vol. 56, no. 4, pp. 1217–1221, Oct. 20, 2018, ISSN: 1429-2955. DOI: 10.15632/jtam-pl.56.4.1217.

[79] D. J. Frew, "Pulse Shaping Techniques for Testing Elastic-plastic Materials with a Split Hopkinson Pressure Bar," *Experimental Mechanics*, vol. 45, no. 2, pp. 186–195, Apr. 1, 2005, ISSN: 0014-4851. DOI: 10.1177/0014485105052111.

[80] R. Naghdabadi, M. Ashrafi, and J. Arghavani, "Experimental and numerical investigation of pulse-shaped split Hopkinson pressure bar test," *Materials Science and Engineering: A*, vol. 539, pp. 285–293, Mar. 2012, ISSN: 09215093. DOI: 10.1016/j.msea.2012.01.095.

[81] W. W. Chen and B. Song, *Split Hopkinson (Kolsky) Bar: Design, Testing and Applications*, ser. Mechanical Engineering Series. New York, NY: Springer, 2011, 388 pp., OCLC: 838266916, ISBN: 978-1-4419-7981-0 978-1-4419-7982-7.

[82] S. E. Rigby, A. D. Barr, and M. Clayton, "A review of Pochhammer–Chree dispersion in the Hopkinson bar," *Proceedings of the Institution of Civil Engineers - Engineering and Computational Mechanics*, vol. 171, no. 1, pp. 3–13, Nov. 8, 2017, ISSN: 1755-0777. DOI: 10.1680/jencm.16.00027.

[83] T. J. Cloete, G. Paul, and E. B. Ismail, "Hopkinson bar techniques for the intermediate strain rate testing of bovine cortical bone," *Philosophical Transactions of the Royal Society A: Mathematical, Physical and Engineering Sciences*, vol. 372, no. 2015, pp. 20 130 210–20 130 210, May 13, 2014, ISSN: 1364-503X, 1471-2962. DOI: 10.1098/rsta.2013.0210.

[84] F. Latourte, Z. Feinberg, L. F. Mori, G. B. Olson, and H. D. Espinosa, "Shear and tensile plastic behavior of austenitic steel TRIP-120 compared with martensitic steel HSLA-100," *International Journal of Fracture*, vol. 162, no. 1-2, pp. 187–204, Mar. 2010, ISSN: 0376-9429, 1573-2673. DOI: 10.1007/s10704-010-9472-y.

[85] A. G. Odeshi, G. M. Owolabi, and M. Nabil Bassim, "Effects of particulate reinforcement and strain-rates on deformation and fracture behavior of Aluminum 6061-T6 under high velocity impact," *Materialwissenschaft und Werkstofftechnik*, vol. 38, no. 2, pp. 66–69, Feb. 2007, ISSN: 09335137, 15214052. DOI: 10.1002/mawe.200600107.

[86] M. Dolinski, M. Merzer, and D. Rittel, "Analytical formulation of a criterion for adiabatic shear failure," *International Journal of Impact Engineering*, vol. 85, pp. 20–26, Supplement C Nov. 1, 2015, ISSN: 0734-743X. DOI: 10.1016/j.ijimpeng.2015.06.009.

[87] M. Štamborská, M. Kvíčala, and M. Losertová, "Identification of the Mechanical Properties of High-Strength Steel Using Digital Image Correlation," *Advanced Materials Research*, vol. 980, pp. 122–126, Jun. 2014, ISSN: 1662-8985. DOI: 10.4028/www.scientific.net/AMR.980.122.

[88] H. Kuhn, Ed., *Mechanical Testing and Evaluation*, [11. ed.], 1. print, ASM Handbook prepared under the direction of the ASM International Handbook Committee ; Vol. 8, OCLC: 248196014, Materials Park, Ohio: ASM International, 2000, 998 pp., ISBN: 978-0-87170-389-7.

[89] A. C. Ugural, S. K. Fenster, and A. C. Ugural, *Advanced Mechanics of Materials and Elasticity*, 5th ed. Upper Saddle River, NJ: Prentice Hall, 2011, 680 pp., ISBN: 978-0-13-707920-9.

[90] J. Schindelin, I. Arganda-Carreras, E. Frise, V. Kaynig, M. Longair, T. Pietzsch, S. Preibisch, C. Rueden, S. Saalfeld, B. Schmid, J.-Y. Tinevez, D. J. White, V. Hartenstein, K. Eliceiri, P. Tomancak, and A. Cardona, "Fiji: An open-source platform for biological-image analysis," *Nature Methods*, vol. 9, no. 7, pp. 676–682, Jul. 2012, ISSN: 1548-7105. DOI: 10.1038/nmeth.2019.

[91] C. A. Schneider, W. S. Rasband, and K. W. Eliceiri, "NIH Image to ImageJ: 25 years of image analysis," *Nature Methods*, vol. 9, no. 7, pp. 671–675, Jul. 2012, ISSN: 1548-7091, 1548-7105. DOI: 10.1038/nmeth.2089.

[92] P. Longère, "Respective/combined roles of thermal softening and dynamic recrystallization in adiabatic shear banding initiation," *Mechanics of Materials*, Oct. 2017, ISSN: 01676636. DOI: 10.1016/j.mechmat.2017.10.003.

[93] A. F. Conn, S. L. Rudy, and S. C. Howard, "THE STRAIN RATE DEPENDENCE OF THREE HIGH STRENGTH NAVAL ALLOYS," Office of Naval Research Department of the Navy, T. R. 7111-1, Jun. 1974, p. 128.

[94] L. Daridon, O. Oussouaddi, and S. Ahzi, "Influence of the material constitutive models on the adiabatic shear band spacing: MTS, power law and Johnson–Cook models," *International Journal of Solids and Structures*, vol. 41, no. 11-12, pp. 3109–3124, Jun. 2004, ISSN: 00207683. DOI: 10.1016/j.ijsolstr.2004.01.008.

[95] R. C. Batra, "Analysis of Adiabatic Shear Bands by Numerical Methods," in *Adiabatic Shear Localization*, Elsevier, 2012, pp. 173–214, ISBN: 978-0-08-097781-2. DOI: 10.1016/B978-0-08-097781-2.00004-6.

[96] S. N. Medyanik, W. K. Liu, and S. Li, "On criteria for dynamic adiabatic shear band propagation," *Journal of the Mechanics and Physics of Solids*, vol. 55, no. 7, pp. 1439–1461, Jul. 1, 2007, ISSN: 0022-5096. DOI: 10.1016/j.jmps.2006.12.006.

[97] S. Li, W. K. Liu, A. J. Rosakis, T. Belytschko, and W. Hao, "Mesh-free Galerkin simulations of dynamic shear band propagation and failure mode transition," *International Journal of Solids and Structures*, vol. 39, no. 5, pp. 1213–1240, Mar. 1, 2002, ISSN: 0020-7683. DOI: 10.1016/S0020-7683(01)00188-3.

[98] P. Molyneux-Berry, C. Davis, and A. Bevan, "The Influence of Wheel/Rail Contact Conditions on the Microstructure and Hardness of Railway Wheels," *The Scientific World Journal*, vol. 2014, pp. 1–16, 2014, ISSN: 2356-6140, 1537-744X. DOI: 10.1155/2014/209752.

[99] L. Jing, L. Han, L. Zhao, and Y. Zhang, "The Dynamic Tensile Behavior of Railway Wheel Steel at High Strain Rates," *Journal of Materials Engineering and Performance*, vol. 25, no. 11, pp. 4959–4966, Nov. 2016, ISSN: 1059-9495, 1544-1024. DOI: 10.1007/s11665-016-2359-y.

[100] U. Zerbst, R. Lundén, K.-O. Edel, and R. Smith, "Introduction to the damage tolerance behaviour of railway rails – a review," *Engineering Fracture Mechanics*, vol. 76, no. 17, pp. 2563–2601, Nov. 2009, ISSN: 00137944. DOI: 10.1016/j.engfracmech.2009.09.003.

[101] M. R. Garcia, "High Speed Rail Crossing with Flange-Bearing Cross Traffic - UPRR/TPW Crossing in Chenoa, IL," p. 12, Sep. 21, 2004.

[102] L. L. Han, L. Jing, H. C. Wei, and Y. Z. Yan, "Experimental Characterization of the Dynamic Compressive Properties of Railway Wheel Steel," *Materials Science Forum*, vol. 867, pp. 29–33, Aug. 2016, ISSN: 1662-9752. DOI: 10.4028/www.scientific.net/MSF.867.29.

[103] E28 Committee, "Test Method for Brinell Hardness of Metallic Materials," ASTM International. DOI: 10.1520/E0010-18.

[104] ——, "Test Methods of Compression Testing of Metallic Materials at Room Temperature," ASTM International. DOI: 10.1520/E0009-09R18.

[105] S. K. Samanta, "Dynamic deformation of aluminium and copper at elevated temperatures," *Journal of the Mechanics and Physics of Solids*, vol. 19, no. 3, pp. 117–135, Jun. 1, 1971, ISSN: 0022-5096. DOI: 10.1016/0022-5096(71)90023-8.

[106] R. Andersson, J. Ahlström, E. Kabo, F. Larsson, and A. Ekberg, "Numerical investigation of crack initiation in rails and wheels affected by martensite spots," *International Journal of Fatigue*, vol. 114, pp. 238–251, Sep. 2018, ISSN: 01421123. DOI: 10.1016/j.ijfatigue.2018.05.023.

[107] J. Xiao, F. Zhang, and L. Qian, "Numerical simulation of stress and deformation in a railway crossing," *Engineering Failure Analysis*, vol. 18, no. 8, pp. 2296–2304, Dec. 2011, ISSN: 13506307. DOI: 10.1016/j.engfailanal.2011.08.006.

[108] A. Marchand and J. Duffy, "An experimental study of the formation process of adiabatic shear bands in a structural steel," *Journal of the Mechanics and Physics of Solids*, vol. 36, no. 3, pp. 251–283, Jan. 1, 1988, ISSN: 0022-5096. DOI: 10.1016/0022-5096(88)90012-9.

Appendix A

Phase 1 Report: Dynamic Compression Testing of Navy Steels

Report prepared for Defence Research and Development Canada on naval steels that were tested in the scope of this thesis.

Prepared by: Michael Conway and James Hogan, University of Alberta
Prepared for: Allison Nolting, Defence Research and Development Canada

Technical Summary

In this report, four materials were tested at elevated strain rates using a Split-Hopkinson Pressure bar. The four materials tested were 350WT, HSLA 65, HY-80, and DH36. The yield strengths found were (1023 ± 21) MPa for 350WT, (1109 ± 50) MPa for HSLA 65, (1149 ± 35) MPa for HY-80, and (1029 ± 23) MPa for DH36. The strain rates achieved were between $1400\,\mathrm{s}^{-1}$ to $1900\,\mathrm{s}^{-1}$. Shear banding was only visually apparent in HSLA 65, with velocities ranging from $862\,\mathrm{m\,s}^{-1}$ to $2470\,\mathrm{m\,s}^{-1}$.

Further, this report includes:

- Testing procedures and operation of the Split-Hopkinson Pressure Bar apparatus.

- Test parameters including all electronics and mechanical systems related to the Split-Hopkinson Pressure Bar.
- Plotted stress-strain curves including the tests respective achieved strain rates.
- Quantitative analysis of the shear band formation (i.e. velocity) on materials that had apparent shear banding occurring on the surface.

Along with this report the electronic data files include:

- In-situ high speed imaging (1–2 million frames per second) of the Split-Hopkinson Pressure Bar tests in `.tiff` and `.avi` format.
- Raw voltage output from all the tests in plain text in delimited format.
- Computed stress, strain, strain rate data in plain text in delimited format.

A.1 Introduction

In Canada, naval steel performance is often determined through bulge testing, Charpy impact testing and quasi-static compression and tension experimentation. While these tests provide performance characteristics of the steel for seaworthiness and combat, understanding the behaviours of these steels in simplified loading conditions can lead to a more fundamental understanding of what governs material performance in extreme environments. For example, bulge testing examines the steel's resistance to crack formation, ductility and toughness on the bulk material for explosive loading, but does not provide details for lower strain rates and simplified compressive stress-states such as wave slamming forces. The Split-Hopkinson pressure bar (SHPB), on the other hand, both allows the study of representative strain rates and stress states while being more readily available to researchers. An added benefit of this testing technique is that it also allows the study of individual failure mechanisms, such as shear bands, that dominate in high strain rate loading [108]. Ultimately, understanding the failure mechanisms will improve materials both designed

and selected for naval application, and explain the current performance in standard tests (e.g. bulge tests).

In this work, the objectives are to test and derive stress and strain data of the selected navy steels using a SHPB. Through this testing with ultra high speed imaging, shear bands may be captured for the tested steels. For the materials that show distinct shear banding, a quantitative analysis will be performed (i.e. velocity).

This report is a summary of the testing procedures, materials tested and results collected using a SHPB. For each material, three tests are conducted and the materials are as follows:

1. MIL-S-16216, HY-80
2. CSA 40.20/40.21 CSA 350WT cat 5 steel
3. ASTM A945/A945M, HSLA 65
4. Lloyd's Register (or equivalent) DH36 steel

A.2 Methods and Procedure

A.2.1 Equipment

The equipment used in this work is as follows:

- **Data Acquisition:** HBM Gen3i
- **Signal Conditioning Amplifier:** Vishay 2310B
- **High Speed Camera:** Shimadzu HPVX-2
- **Lighting:** REL Ring Light
- **Testing Apparatus:** Split-Hopkinson Pressure Bar

The data acquisition was set at 25 MHz and the Shimadzu HPVX-2 was recording 128 frames at 1 or 2 million frames per second with a resolution of (400×250) pixels.

Split-Hopkinson Pressure Bar Apparatus

The dynamic compression tests of the navy materials were performed with a Split-Hopkinson Pressure Bar apparatus. The striker, incident and transmission bars were 12.7 mm in diameter and made of Maraging C350 steel that was heat treated to obtain a minimum hardness of 52 Rc. The three bars in the apparatus included a 304 mm striker, 914.4 mm incident bar and a 1016 mm transmission bar. The SHPB apparatus can be seen in Figure A.1.

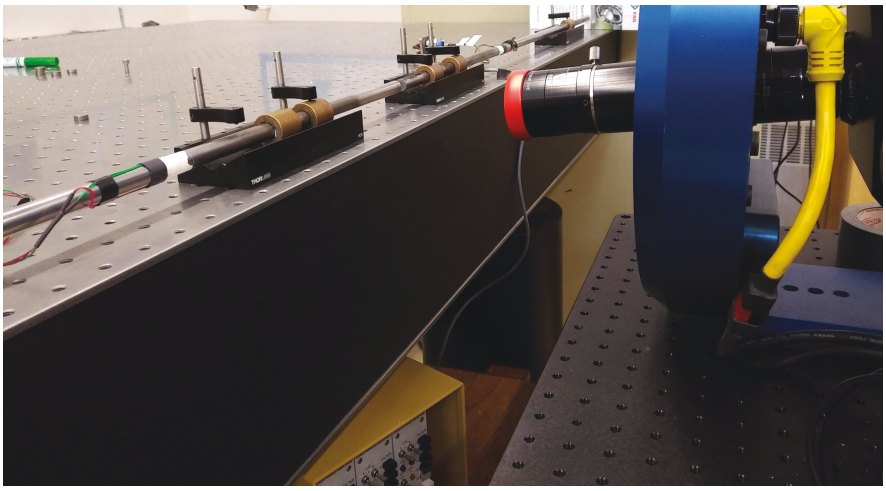

Figure A.1. Split-Hopkinson Pressure Bar used for testing.

The data was processed using eqs. (A.1) to (A.3):

$$\dot{\varepsilon}_s = -2\frac{C_B}{L_s}\varepsilon_r \tag{A.1}$$

$$\varepsilon_s = -2\frac{C_B}{L_s}\int_0^t \varepsilon_r \, \mathrm{d}t \tag{A.2}$$

$$\sigma_s = \frac{A_B}{A_s}E_B\varepsilon_T \tag{A.3}$$

In Equations (A.1) to (A.3), $\dot{\varepsilon}_s$ was the strain rate in the specimen (s^{-1}), C_B was the elastic wave speed in the incident and transmission bars ($\mathrm{m\,s}^{-1}$), L_s was the length of the specimen (m), and E_B was the elastic modulus of the bar (GPa). The value of the elastic modulus of Maraging C350 is 199 GPa. The area is represented by, A, and the strain calculated from the voltage signal,

ε. These follow the subscripts of r for the reflected wave, T for the transmitted wave, s for the specimen, and B for the bars. Stress equilibrium was achieved by obtaining a constant strain rate. Stress equilibrium was achieved through proper specimen design and pulse shaping. Verification of stress equilibrium was performed through a force balance, which was found in agreement for our tests and can be found seen in Section A.6.

A.2.2 Specimen Preparation

The samples for the SHPB tests were machined from center of the thickness of the as-received plate in the orientation seen in Figure A.2. The samples were prepared through milling, subsequent grinding for parallelism and polishing of all faces. The tolerances and preparation follow ASTM E9 [104]. The drawing for manufacturing the specimen is shown in Section A.5.

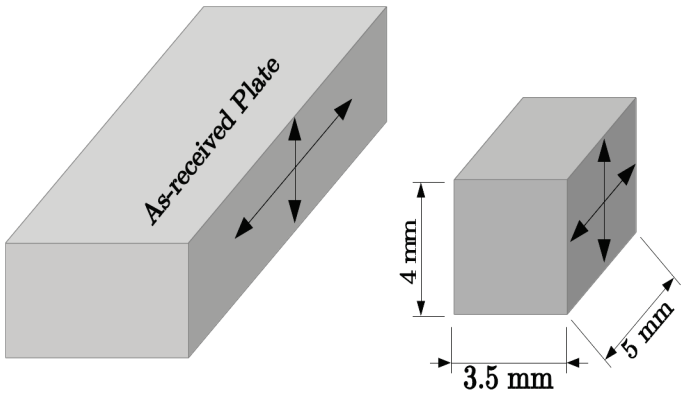

Figure A.2. The location and orientation of the extraction of the specimens from the as-received plate.

The specimens were chosen to be rectangular prisms in order to have a flat surface for imaging. The length of each size was chosen in order to meet the required strain rate in the order of 10^3 and to provide a length to area ratio to minimize dispersion of the waves. Typically, cylindrical specimens are used for symmetry, but symmetry is often broken when localizations initiate, therefore less important in the case of specifically studying shear banding in materials.

A.2.3 Procedure

The testing procedure was as follows:

1. All electronics (amplifiers, data acquisition and high speed camera) are turned on and allowed to warm to operating temperatures.
2. Specimens and pulse shapers dimensions were measured, recorded and labelled.
3. Interfaces of the bars with the pulse shaper and specimen were cleaned with acetone to remove previously applied grease and contaminants.
4. Specimen is placed between the incident and transmission bar with a small amount of high pressure grease.
5. Pulse shaper is placed on the incident bar where striker impacts with a small amount of high pressure grease on a marked center.
6. Projectile is loaded and the gas gun is primed to a specified pressure (see Section A.7).
7. Projectile is fired.
8. High speed imaging system is triggered via the Data acquisition system.
9. Data from the acquisition system and high speed images are exported to the hard disk drive.
10. The exported data and images are then checked for data integrity by taking the SHA-256 checksum to ensure data was not corrupted in data transfer.
11. The data was processed following Section A.2.1, in order to calculate stress and strain.
12. Item 3 to item 11 are then repeated for the remaining tests.

The relevant settings and specimen measurements are attached in Section A.7.

A.3 Results

A.3.1 HSLA 65

Three tests were performed on the HSLA 65 material. The stress-strain curves generated are shown in Figure A.3. The calculated yield strength and yield strain are summarized in Table A.1. The yield stress and strains were taken from the sharp knee in the stress strain plot and the average stress and strain is also calculated to show variability between the tests.

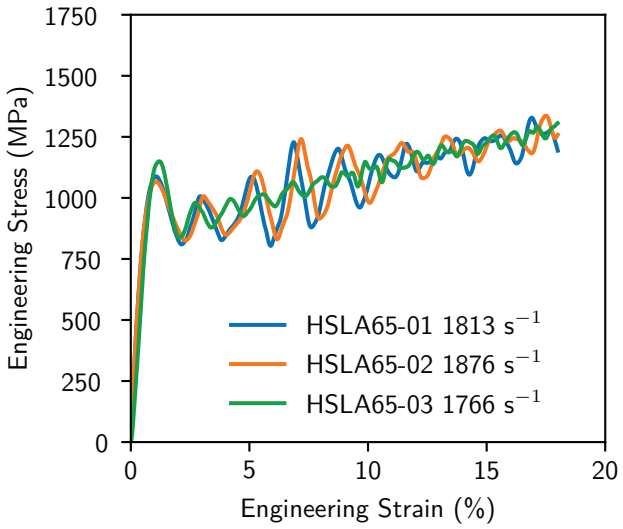

Figure A.3. HSLA 65 stress-strain curve in dynamic compression using a Split-Hopkinson Pressure Bar apparatus.

Table A.1. HSLA 65 yield strength and yield strain for all tests conducted on HSLA 65.

Test Number	Yield Strength (MPa)	Yield Strain (%)
1	1,092	1.05
2	1,069	1.06
3	1,165	1.22
Average	1,109	1.11
Std. Dev.	50	0.09

Images taken with the Shimadzu HPVX-2 at 2 million frames per second for "Test 1" and "Test 2" are shown in Figures A.4 and A.5, respectively. The surface deformation was recognized as shear bands and were clearly seen in two

of the three tests conducted. The velocity measurements were taken during the initial phase of development before clear coalescence was seen. The velocity of the shear band was taken to be the dark line like feature formation on the surface of the between frames. The total length travelled is then divided by the time difference between frames (500 ns).

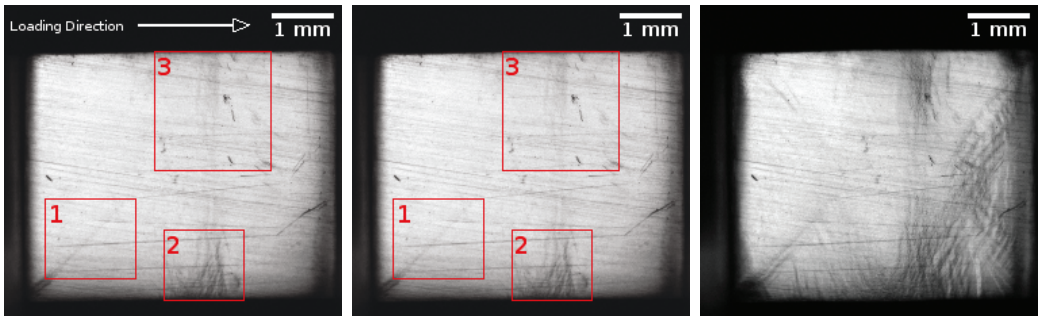

(a) (b) (c)

Figure A.4. HSLA 65 in "Test 1" in dynamic compression ($\dot{\varepsilon}$ =1813 s^{-1}) at 2 million frames per second where the labelled 1, 2 and 3 zones are referenced to Table A.2: (a) is the sample in undeformed state, (b) at the beginning of shear band growth (2.1% strain), (c) the surface of the sample at 5.2% strain.

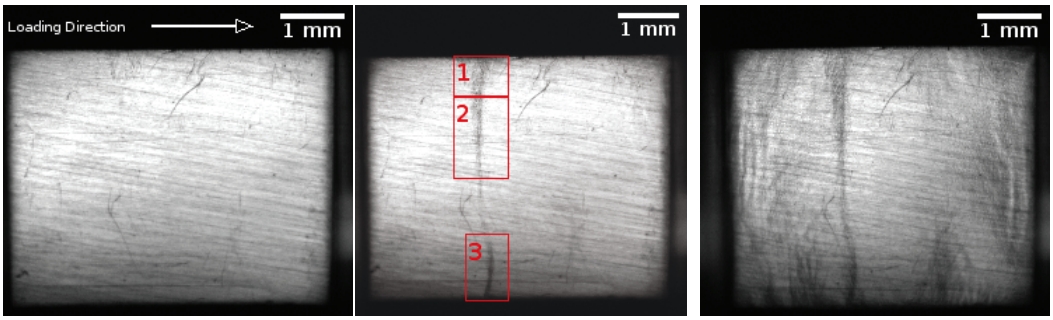

(a) (b) (c)

Figure A.5. HSLA 65 in "Test 2" in dynamic compression ($\dot{\varepsilon}$ =1876 s^{-1}) at 2 million frames per second where the labelled 1, 2 and 3 zones are referenced to Table A.2: (a) is the sample in undeformed state, (b) at the beginning of shear band growth (2.2% strain), (c) the surface of the sample at 4.8% strain.

From the two tests and the marked three zones the shear band velocities are summarized in Table A.2. The values are measured over three frames.

Table A.2. Shear band velocities (propagation of line like surface features during deformation) measured in the respective zones identified in the images for "Test 1" and "Test 2" on HSLA 65

	Zone	Velocity (m/s)
Test 1	1	948
		1802
	2	862
		1800
		1196
	3	1498
		2032
Test 2	1	982
	2	2470
	3	1518

A.3.2 HY-80

Similarly, three tests were performed on HY-80. The stress-strain curve are given in Figure A.6 with the yield strengths and yield strains summarized in Table A.3. Again, the yield strength is taken at the sharp knee point.

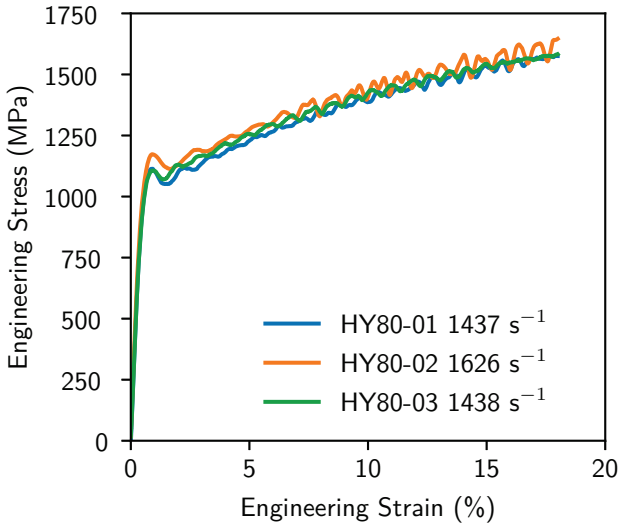

Figure A.6. HY-80 stress-strain curve in dynamic compression using a Split-Hopkinson Pressure Bar apparatus

Table A.3. HY-80 yield strength and yield strain for all tests conducted on HY-80

Test Number	Yield Strength (MPa)	Yield Strain (%)
1	1,135	0.86
2	1,189	0.85
3	1,124	0.93
Average	1,149	0.88
Std. Dev.	35	0.05

The high speed images from "Test 2" are provided in Figure A.7. In this material shear banding is not apparent on the surface of the specimen. Instead we can see a progression of surface texturing occurring on the surface from left to right. For example, the small dimple features in the top right hand corner of Figure A.7c. The three images were selected to show the undeformed surface of the specimen, at the point of surface texturing beginning and later on in the deformation of the material.

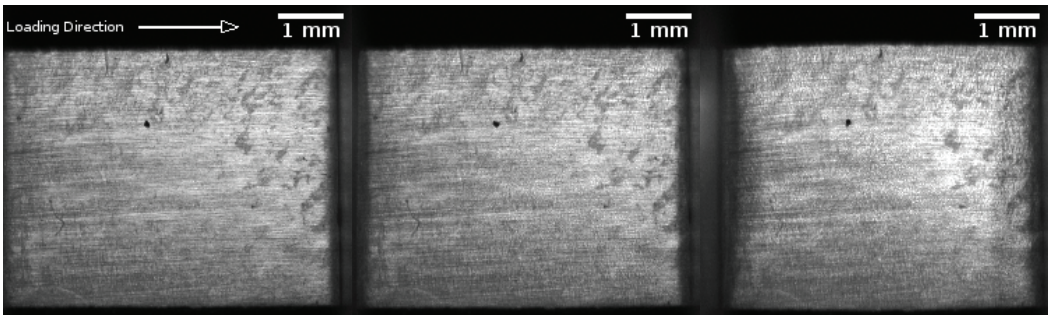

(a) (b) (c)

Figure A.7. HY-80 in "Test 2" in dynamic compression at strain rates of approximately $1626\,s^{-1}$ using the Shimadzu HPVX-2 at 1 million frames per second: (a) is the sample in undeformed state, (b) at the beginning of surface texturing (1.9% strain), (c) the surface of the sample at 4.9% strain.

A.3.3 350WT

Three tests were performed on 350WT and the stress-strain curve is given in Figure A.8. The yield strengths and strains are summarized in Table A.4.

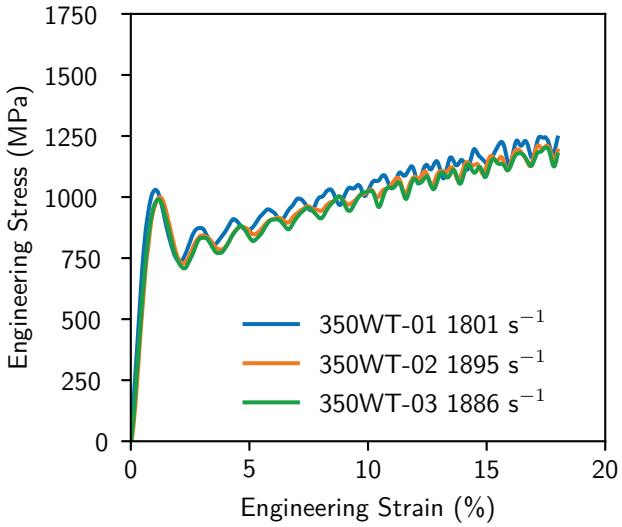

Figure A.8. 350WT stress-strain curve in dynamic compression using a Split-Hopkinson Pressure Bar apparatus

Table A.4. 350WT yield strength and yield strain for all tests conducted on 350WT

Test Number	Yield Strength (MPa)	Yield Strain (%)
1	1,047	1.08
2	1,014	1.26
3	1,008	1.19
Average	1,023	1.17
Std. Dev.	21	0.09

Three images are taken from the high speed videos. In these images there is no apparent shear banding on the surface. Slight surface texturing is seen developing from left to right, where the left most image is the undeformed surface and the right most image is at 5% strain.

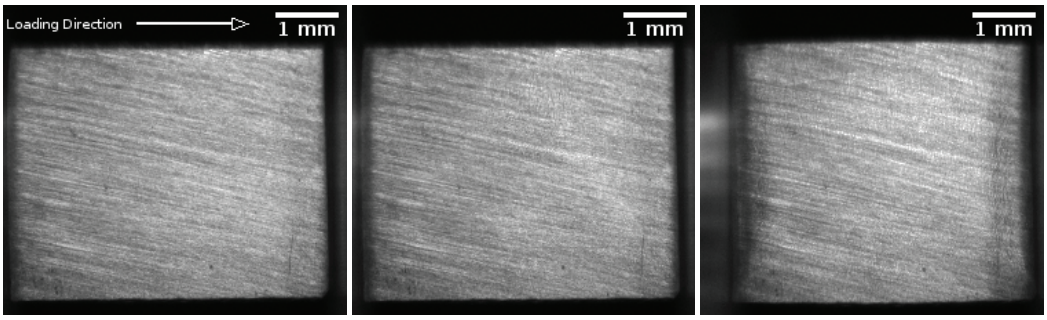

Figure A.9. 350WT in "Test 1" in dynamic compression at strain rates of approximately $1801\,s^{-1}$ using the Shimadzu HPVX-2 at 2 million frames per second: (a) is the sample in undeformed state, (b) at the beginning of shear band growth with the zones where measurements were taken marked (1.8% strain), (c) the surface of the sample at 5% strain.

A.3.4 DH36

Three tests were completed on DH36 and the stress-strain curves are provided in Figure A.10. The yield strength and strain are summarized in Table A.5.

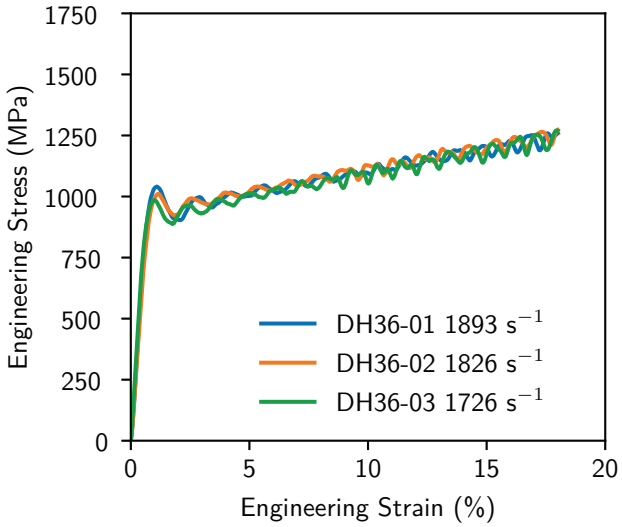

Figure A.10. DH36 stress-strain curve in dynamic compression using a Split-Hopkinson Pressure Bar apparatus

Table A.5. DH36 yield strength and yield strain for all tests conducted on DH36

Test Number	Yield Strength (MPa)	Yield Strain (%)
1	1,055	0.99
2	1,025	1.23
3	1,008	1.00
Average	1,029	1.07
Std. Dev.	23	0.14

Similarly as before, three images are provided from the high-speed camera. There is again no apparent shear banding on the surface of the material. Instead three images of the undeformed sample to 5% strain is shown with a progress of surface texturing.

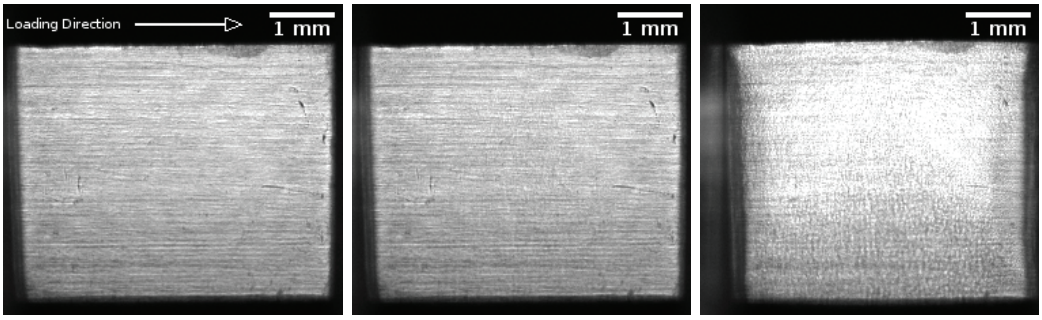

Figure A.11. DH36 in "Test 2" in dynamic compression at strain rates of approximately $1826\,s^{-1}$ using the Shimadzu HPVX-2 at 1 million frames per second: (a) is the sample in undeformed state, (b) at the beginning of surface texturing (0.9% strain), (c) the surface of the sample at 5% strain.

A.3.5 Comparison

To compare the performance of the materials, a representative stress-strain curve from each material is plotted in Figure A.12. All the yield strength and the yield strains for the materials tested in this report are summarized in Table A.6. It can be seen that all of the materials are similar in yield strength. Secondly, the average strain rate of the HY-80 is lower, this indicates that it is a stiffer material and the strain hardening is seen to be higher than the other materials. Lastly, it appears that HY-80 has the highest yield strength and hardens at the greatest rate after yield. Conversely, the 350WT has the lowest yield strength and the largest amount of softening post yield.

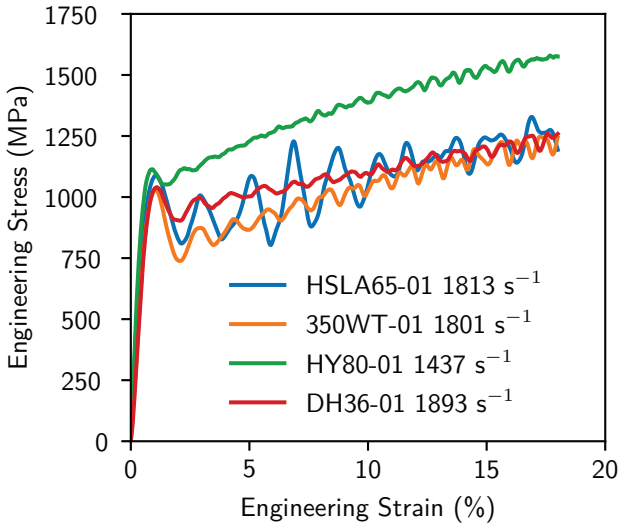

Figure A.12. A representative stress-strain curves of each different naval steel material in this document in dynamic compression.

Table A.6. Yield stress and yield strain for all four materials tested.

Material	Yield Stress (MPa)	Avg. Yield Strain(%)
350WT	1023 ± 21	1.17 ± 0.09
HSLA 65	1109 ± 50	1.11 ± 0.09
HY-80	1149 ± 35	0.88 ± 0.05
DH36	1029 ± 23	1.07 ± 0.14

A.4 Conclusion

From the tests conducted, it can be seen that the materials selected here have similar yield strength performance at elevated strain rates in compressive loading. In the future, it would be beneficial to examine the quasi-static compressive behaviour to better understand the strain-rate dependence of each material. The only material to exhibit apparent shear banding on the surface was HSLA 65 with the shear band speeds ranging from $862\,\mathrm{m\,s^{-1}}$ to $2470\,\mathrm{m\,s^{-1}}$. The other materials do not exhibit clear shear banding and instead surface texturing is the dominant visual feature.

A.5 Specimen Drawing

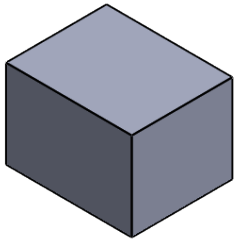

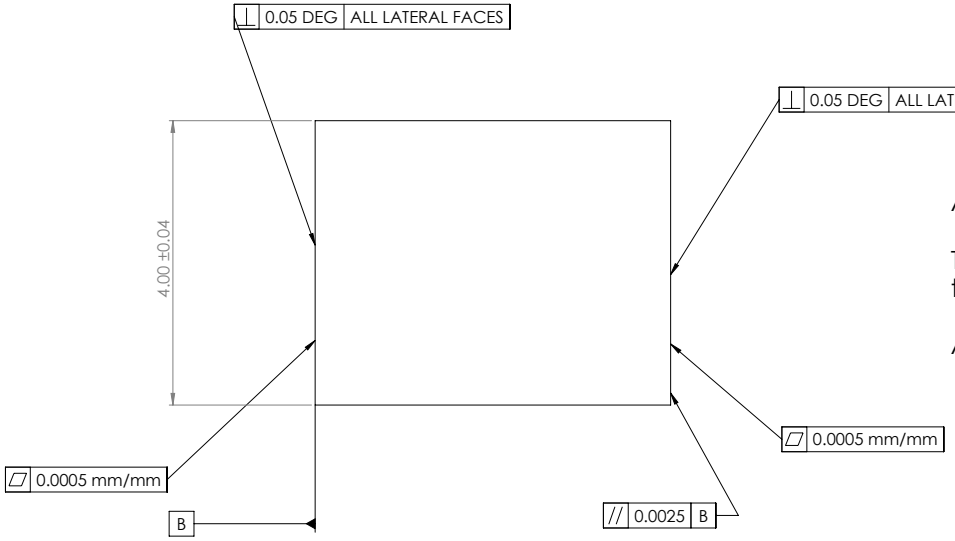

All surfaces to be finished to less than 1.6 µm RA.

The opposing 5.00 mm x 4.00 mm sides surface finish to be polished to < 0.1 µm RA

All edges to be deburred

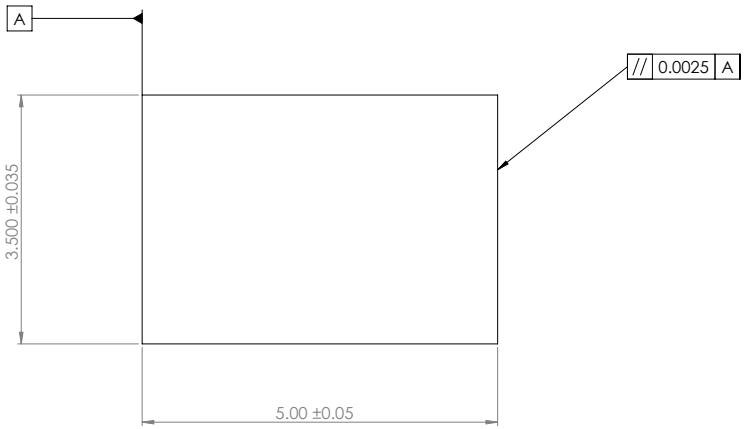

UNLESS OTHERWISE SPECIFIED: DIMENSIONS ARE IN MILLIMETERS SURFACE FINISH: 1.6 µm TOLERANCES: LINEAR: - ANGULAR: -				DO NOT SCALE DRAWING	REVISION B
	NAME	SIGNATURE	DATE	TITLE: Large Specimen Blocks	
DRAWN	Michael Conway		20/07/2016		
CHK'D					
APPV'D					
MFG					
Q.A				DWG NO. LG-BLK	A2
			WEIGHT:	SCALE:20:1	SHEET 1 OF 1

A.6 Test Quality Verification

The quality of the SHPB tests was verified by assessing the quality of the force balance and achieving a constant strain rate. The quality of the force balance is determined through the value of the incident wave minus the reflected and transmitted waves being close to zero throughout the test. In the tests conducted in this report, the difference is minimal and a representative plot can be found in Figure A.13.

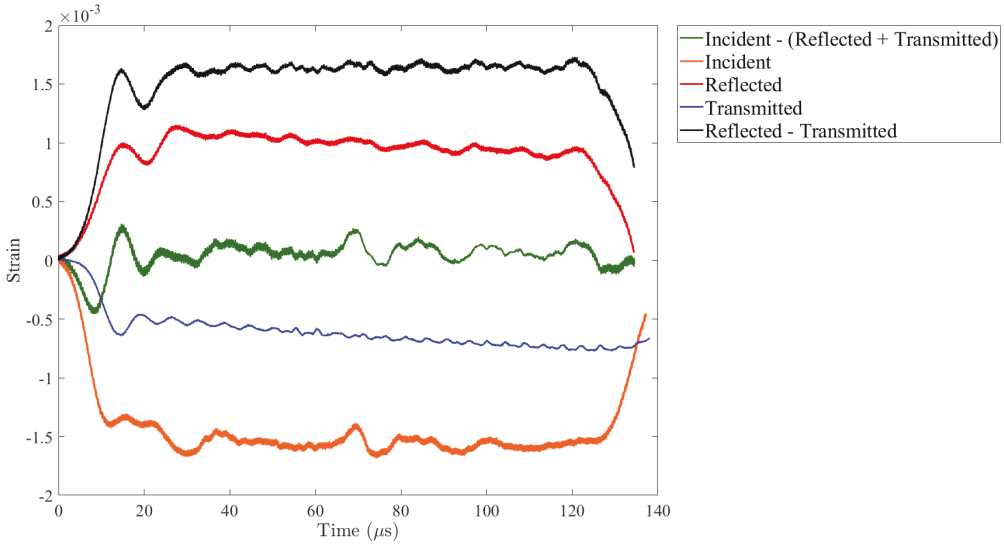

Figure A.13. Force balance of the SHPB tests through comparing the stress waves before and after the specimen for HSLA 65: "Test 1".

Secondly, the plot of the strain rate against time is shown in Figure A.14. In this plot it can be seen that the values plateau to a approximately constant value of approximately $1800\,\mathrm{s}^{-1}$ for the entire duration of the test.

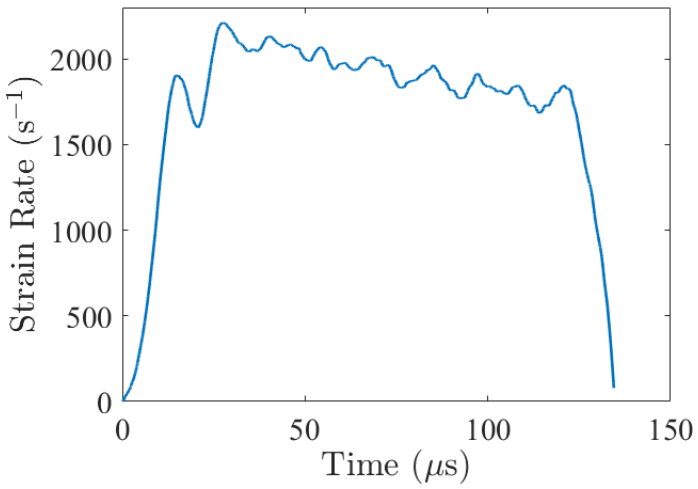

Figure A.14. Strain rate of the specimen during the SHPB test for HSLA 65: “Test 1”.

A.7 Electronic and Mechanical Testing Parameters

Test ID	Material	Date	Test Number	Time of Test	Camera File	Trigger Delay (ns)	Trigger Frame
1	DH36	2/20/2019	1	13:20:23	13_20_24	76000	5
2	DH36	2/20/2019	2	13:56:30	13_56_31	116000	2
3	DH36	2/20/2019	3	14:10:03	14_10_03	110000	2
4	HSLA65	2/20/2019	3	14:27:59	14_27_59	110000	2
5	HY80	2/20/2019	1	16:14:55	14_27_59	110000	2
6	HY80	2/20/2019	2	16:36:49	14_27_59	110000	2
7	HY80	2/20/2019	3	16:51:57	14_27_59	110000	2
8	350WT	2/20/2019	1	17:09:37	14_27_59	110000	2
9	350WT	2/20/2019	2	17:26:25	14_27_59	110000	2
10	350WT	2/20/2019	3	17:50:43	14_27_59	110000	2
11	HSLA65	10/24/2018	1	16:23:14	16_22_40	--	--
12	HSLA65	10/24/2018	2	16:34:30	16_32_05	--	--

Live Rec Delay (ns)	Exposure (ns)	Rec Speed (ns)	Frame Rate (fps)	Firing Pressure (psi)	Specimen Shape
850	400	1000	1.00E+06	45	Rectangular
850	400	1000	1.00E+06	45	Rectangular
850	400	1000	1.00E+06	45	Rectangular
850	400	1000	1.00E+06	45	Rectangular
850	400	1000	1.00E+06	45	Rectangular
850	400	1000	1.00E+06	45	Rectangular
850	400	1000	1.00E+06	45	Rectangular
850	400	1000	1.00E+06	45	Rectangular
850	400	1000	1.00E+06	45	Rectangular
850	400	1000	1.00E+06	45	Rectangular
--	--	500	2.00E+06	50	Rectangular
--	--	500	2.00E+06	50	Rectangular

Specimen Height (mm)	Specimen Width (mm)	Specimen Length (mm)	Pulse Shaper Thickness (mm)
3.973	3.468	5.001	0.61
3.989	3.489	5.039	0.612
3.977	3.466	5.003	0.614
4.003	3.495	5.008	0.698
4.011	3.516	5.037	0.685
4.003	3.519	5.02	0.656
4.01	3.48	5.037	0.666
4.018	3.524	5.016	0.664
4.013	3.52	5.022	0.669
4.052	3.493	5.037	0.677
4.015	3.497	5.014	0.638
4.009	3.501	5.011	0.667

Pulse Shaper Diameter (mm)	Pulse Shaper Material	Bar Diameter (mm)	Projectile Length (mm)
6.449	Mild Steel	12.7	304
6.473	Mild Steel	12.7	304
6.469	Mild Steel	12.7	304
6.458	Mild Steel	12.7	304
6.408	Mild Steel	12.7	304
6.464	Mild Steel	12.7	304
6.456	Mild Steel	12.7	304
6.466	Mild Steel	12.7	304
6.464	Mild Steel	12.7	304
6.466	Mild Steel	12.7	304
6.464	Mild Steel	12.7	304
6.465	Mild Steel	12.7	304

Incident Bar Length (mm)	Transmitted Bar Length (mm)	Bar Material	Acquisition Rate (MHz)
914.4	1016	Maraging C350	25
914.4	1016	Maraging C350	25
914.4	1016	Maraging C350	25
914.4	1016	Maraging C350	25
914.4	1016	Maraging C350	25
914.4	1016	Maraging C350	25
914.4	1016	Maraging C350	25
914.4	1016	Maraging C350	25
914.4	1016	Maraging C350	25
914.4	1016	Maraging C350	25
914.4	1016	Maraging C350	20
914.4	1016	Maraging C350	20

Channel 1 Gain	Channel 2 Gain	Channel 3 Gain	Channel 4 Gain
10	10	N/A	1
10	10	N/A	1
10	10	N/A	1
10	10	N/A	1
10	10	N/A	1
10	10	N/A	1
10	10	N/A	1
10	10	N/A	1
10	10	N/A	1
10	10	N/A	1
10	10	N/A	1
10	10	N/A	1
10	10	N/A	1

Distance to Strain Gauge 1 (mm)	Distance to Strain Gauge 2 (mm)
698.5	317.5
698.5	317.5
698.5	317.5
698.5	317.5
698.5	317.5
698.5	317.5
698.5	317.5
698.5	317.5
698.5	317.5
698.5	317.5
660	360
660	360

Distance to Strain Gauge 3 (mm)	Gauge Factor	Excitation Voltage
317.5	2.15	10
317.5	2.15	10
317.5	2.15	10
317.5	2.15	10
317.5	2.15	10
317.5	2.15	10
317.5	2.15	10
317.5	2.15	10
317.5	2.15	10
317.5	2.15	10
360	2.15	15
360	2.15	15